2018-01-01

Magnetic And Catalytic Properties Of Transition Metal Doped MOS2 Nanocrystals

Luis Martinez
University of Texas at El Paso, lmmartinez12@miners.utep.edu

MAGNETIC AND CATALYTIC PROPERTIES OF TRANSITION METAL DOPED MoS_2 NANOCRYSTALS

LUIS MIGUEL MARTINEZ MILIAN

Master's Program in Physics

APPROVED:

Srinivasa Rao Singamaneni, Ph.D., Chair

Russell Chianelli, Ph.D.

Harikrishnan Nair, Ph.D.

Charles H. Ambler, Ph.D.
Dean of the Graduate School

MAGNETIC AND CATALYTIC PROPERTIES of TRANSITION METAL DOPED MoS_2 NANOCRYSTALS

by

LUIS MIGUEL MARTINEZ MILIAN, B.S.

THESIS

Presented to the faculty of the Graduate School of

The University of Texas at El Paso

in Partial Fulfillment

of the Requirements

for the Degree of

MASTER OF SCIENCE

Department of Physics

THE UNIVERSITY OF TEXAS AT EL PASO

May 2018

Acknowledgements

L. M. M. acknowledges Dr. H. Nair and Dr. R. Chianelli for kindly agreeing to be a part of this Thesis committee. L. M. M. acknowledges support from UTEP start-up grant. L. M. M. also acknowledges the Wiemer Family for awarding Student Endowment for Excellence and also the NSF-PREM program. L. M. M. acknowledges that part of the magnetic work performed at Ames Laboratory by I. C. Nlebedim and K. Gandha. L. M. M. acknowledges the collaboration and TEM work performed by D. Chinnathambi at Boise State University. L. M. M. acknowledges the collaboration performed by D. Villagran and Y. Wu for the electrocatalytic measurements. L. M. M. acknowledges R. R. Chianelli for helpful discussion and for laboratory access and use of equipment. L. M. M. would like to thank S. Hennadige for help in taking EPR spectroscopy measurements. L. M. M. would like to thank J. Delgado for help with the electrocatalytic measurements and synthesis of materials. L. M. M. thanks A. Cosio for help in the analysis of the magnetic measurements and synthesis of materials. L. M. M. thanks C. Saiz for help in preparation of the $FeMoS_2$ NCs samples. Finally, L. M. M. would like to thank Dr. S. R. Singamaneni for the mentorship and all his help throughout my M.S. in Physics.

Abstract

Magnetism and catalytic activity of nanoscale layered two-dimensional (2D) transition metal dichalcogenides (TMDs) have gained an increasing research interest in the recent past. To broaden the current knowledge and understanding on this subject, in this work, together with my collaborators, I study the magnetic and electrocatalytic properties of hydrothermally grown pristine and transition metal doped (10% of Co, Ni, Fe and Mn) 2H-MoS_2 nanosheets/nanocrystals (NCs), with the particle size of 25-30 nm. A broad range of experimental measurements such as x-ray diffraction, transmission electron microscopy, x-ray photo absorption spectroscopy, Raman spectroscopy, magnetic, catalytic and electron spin resonance have been employed to characterize these materials. It has been shown that the room temperature magnetic properties of these nanostructures strongly depend on the nature of dopant, in which, Co, Ni, and Fe doping produces characteristic room temperature ferromagnetism, whereas, Mn doping exhibits stronger paramagnetic features. All the materials showed features related to canted antiferromagnetism at lower temperatures. Among all, Co doped MoS_2 NCs showed stronger catalytic activity and Mn doped MoS_2 NCs showed weaker catalytic activity. These experimental findings combined with electron spin resonance measurements infer that the increasing number of catalytically active sites in Co doped MoS_2 NCs might be responsible for its superior electrocatalytic activity. The present results show that the magnetic order-disorder behavior and catalytic activity can be modulated by choosing the suitable dopants in NCs of 2D materials.

Table of Contents

List of Tables

List of Figures

Chapter 1: Introduction and Motivation

In recent years, an increasing number of scientific studies have been reported for nanoscale two-dimensional (2D) layered transition metal dichalcogenides (TMDs) [1-3]. Interestingly, nanoscale TMDs exhibit new properties and applications upon 2D confinement and have been widely researched for applications such as photodetectors, transistors, catalysts and spintronics [4-9]. Out of all, layered molybdenum disulfide (MoS_2), held together by the van der Waals forces is of particular interest. One of the properties of this material is its ability to tune its direct band gap of 1.2 eV (bulk) to an indirect band gap of 1.8 eV (monolayer), due to quantum confinement and interlayer interaction [4, 10]. In addition, bulk crystals of MoS_2 and WS_2 have been rigorously studied as catalysts for the hydrodesulfurization (HDS) process in the petroleum industry. In particular, MoS_2 is one of the most widely used industrial catalysts for HDS, and is known to be a hydrogen evolution reaction (HER) catalyst [11]. In terms of the Gibbs free energy for hydrogen absorption from the Sabatier principle, MoS_2 can be as good a catalyst as Pt. If the appropriate synthetic modifications are met, MoS_2 could emerge as a competitive candidate for the HER [12]. *The question that then begs to be asked is, where does the catalytic activity come from?*

There has been an increase in attention towards realizing 2D dilute magnetic semiconductors (DMS) for spintronic applications. Theoretical predictions show that magnetism in TMD nanostructures can be realized through doping with various transition metals. Bulk MoS_2 is a semiconductor known to be diamagnetic in nature, but the material can display ferromagnetism when it is prepared in the form of nanostructures. The ferromagnetism found in MoS_2 nanostructures may be due to magnetic moments coming from zigzag edges and sulfur vacancies [16, 17]. Induced magnetism in MoS_2 has also been shown to be achieved by structural phase transition, via Li intercalation [18]. Theoretical calculations performed by Wang and co-authors

predicted the effect of TM doping on the TMDs' magnetic properties. Their work showed how the activity of this cheap, earth-abundant catalyst can be further improved by incorporating TMs, modifying the activity of the S-edge [13]. Other theoretical groups have also shown [19] that doping TMs into MoS_2 can lead to enhanced magnetic properties. While realizing theoretical predictions, few experimental observations have appeared [16, 21] in the literature reporting on magnetic properties of hydrothermally grown TM doped MoS_2 nanostructures. While there are reports on experimental studies on the magnetic properties of TMD nanocrystals (NCs), these studies are limited and at the nascent stage. To broaden the current knowledge and understanding of the doping induced magnetic properties in TMD NCs, an extensive experimental study is required, which is one of the goals of the current Thesis.

Theoretical [13] and experimental [10, 14] studies have shown that the edges and S-vacancies in MoS_2 nanolayers make significant contributions to the electrocatalytic properties, while the basal planes remain inert. Xu *et al* was able to demonstrate a simple strategy to acquire monolayer MoS_2 with S vacancies, and enhanced the electrocatalytic performance [10]. The catalytic activity can also be improved by doping transition metals into MoS_2, as shown by DFT calculations [13]. Defect engineering then has become one method of advancing MoS_2's catalytic activity for the HER. A study performed by X. Dai *et al*, where doping Fe, Ni, and Co into MoS_2 and coating the material with carbon, found incredible catalytic enhancements (with a current density of 60.9 mA/cm^2 at $\eta = 200$ and a Tafel slope of 50 mV/dec) [15]. This was argued to be due to the formation of CoMoS phase (for the case of Co), which provided synergistic regulations between the existence of abundant defects, a balance of active sites and electronic conductivity. These are some of the reports published to further improve MoS_2's catalytic properties. The second

goal of this work is to study the electrocatalytic properties of MoS_2 NCs and the doped (Co, Ni, Fe and Mn) counterparts.

Various methods have been employed to synthesize 2D TMD NCs for the study of their magnetic and catalytic properties. One of the greatest challenges is producing MoS_2 with a rich number of active sites in an efficient and commercially viable way. To achieve monolayers or few layer TMDs, some routes have been developed, including chemical vapor deposition (CVD) [20], chemical exfoliation [18], and micro-mechanical cleavage [21]. The CVD method requires harsh growth conditions, such as high temperatures and high vacuum, which makes this route commercially unviable. The micro-mechanical cleavage method is limited by the low yield of monolayers produced and contain increasing number of unwanted foreign impurities. Lastly, chemical exfoliation requires various lengthy steps (24 hrs. or more) and is extremely sensitive to the environment [22]. On the other hand, a bottom-up approach such as the hydrothermal method is convenient and a low cost route for large-scale synthesis of TMD based NCs and their composites [14]. It is a very simple, efficient, and inexpensive technique used to produce MoS_2 nanostructures. For example, Ahmed *et al* used the hydrothermal method to produce MoS_2 nanosheets and doped the material with (2.5 and 5%) vanadium. Doing this, Ahmed and co-authors were able to induce enhanced magnetism on the MoS_2 nanosheets [4]. Similarly, Xu *et al* was able to develop a simple and effective strategy, using the hydrothermal method, to acquire monolayer MoS_2 with S vacancies [14]. Xu was able to enhance the electrocatalytic activity of MoS_2, enabling the inert basal plane, by introducing localized donor states.

In this study, hydrothermally grown MoS_2 NCs were synthesized and doped (10%) with transition metal ions (Co, Ni, Fe, and Mn). This work identifies the paramagnetic point defects present in hexagonal MoS_2 NCs (2H phase) and the effect of doping on the magnetic properties

using the electron paramagnetic resonance (EPR) spectroscopy and magnetic measurements. Additionally, the study of the catalytic activity of this material is performed for the HER.

Chapter 2: Materials and Methods

MoS_2 NCs were synthesized using a common, facile, bottom-up hydrothermal method [23, 24]. All the precursors are used here as purchased from Alfa Aeser without further purification. In a typical synthesis, 0.4 g of Na_2MoO_4-$2H_20$ was dissolved in 30 mL of deionized (DI) water under sonication for 20 min. At this step the desired metal precursor is added. Then 0.38 g of dibenzyl disulfide was added to the solution along with 30 mL of ethanol and sonicated again for 30 min. The solution was then transferred into a 100 mL teflon-lined stainless steel autoclave and was maintained at 250^o C for 18 hrs. The reaction system was then allowed to cool down to room temperature naturally. The mother liquor was discarded and the collected products were centrifuged for 1 hour and later washed with DI water. Then the stoichiometric MoS_2 NCs were filtered and left to dry in vacuum over night at room temperature. Using this approach, 10% Co, Ni, Fe and Mn doped MoS_2 NCs have been prepared.

For XRD characterizations, an automated Bruker D8 Advance X-ray diffractometer, in the θ-2θ configuration with the Cu kα X-ray radiation was employed. The mean crystallite size was estimated using the Scherrer equation. TEM specimens were prepared by dispersing the powders on holey carbon grids. TEM studies were carried out using a JEOL JEM 2100 HR operated at 200kV. TEM studies were conducted in collaboration with Dr. Karthik Chinnathambi at Boise State University. Raman measurements were performed using a SmartRaman spectrometer from Thermo Scientific with an excitation wavelength of 532 nm. XPS measurements were collected on a Physical Electronics Versa probe using micro-focused monochromatic A1 Kα X-Ray (1486.7 eV) source with a pass energy of 23.5 eV at a 45^o take-off angle. The X-ray source spot size was about 100 μm and the spectral resolution was 0.2 eV. Spectra from the MoS_2 samples were charge corrected by shifting the recorded scans to adventitious carbon (C1s) peak at 284.4 eV. XPS data

were collected by Dr. Madhu Kongara at Boise State University. The magnetization measurements were performed using a Quantum Design PPMS (5-300 K, ±5T). During the magnetic measurements, all the samples are carefully handled with nonmagnetic capsules and tapes to avoid contamination. Most of the magnetic measurements were conducted in our group at UTEP. In addition, we collaborated with Dr. Ikenna's group at Ames Research Laboratory for conducting part of the magnetic measurements.

Catalytic properties were studied in collaboration with Dr. Villagran's group at UTEP Chemistry. All catalysts were accessed heterogeneously for hydrogen production. Prior to electrochemical studies, the catalysts were deposited on a conductive fluorinated-tin oxide (FTO) substrate, with a conductive adhesive silver paste to better support the catalyst. FTO glass was cleaned by sonication in acetone, isopropyl alcohol, and DI water, separately. The silver paste was then coated on top of the active side of the FTO with an area of 0.25 cm^2 (0.5 cm x 0.5 cm). 0.5 mg of the catalyst was dispersed in 1mL of ethanol and sonicated for 30 min. to form a homogenous ink. Then, 10 µL of the catalyst ink was drop cast on the silver paste and the plate was allowed to dry in ambience and was later used as the working electrode for the electrochemical measurements. All electrochemical studies were performed on a CHI760D potentiostat with a three-electrode electrochemical cell in room temperature. A platinum wire was utilized as the counter electrode while a saturated calomel electrode (SCE) was used as the reference electrode. All potentials displayed in this Thesis were referred to as reversible hydrogen electrode (RHE) by adding a value of (0.245 + 0.059 pH) to the data obtained using a SCE reference electrode. An aqueous solution of 0.5 M H_2SO_4 was used as both the proton source and electrolyte. The solution was saturated with nitrogen gas to remove the dissolved oxygen prior to each measurement.

Electrical impedance spectroscopy (EIS) was obtained at different overpotentials from 100 KHz to 0.1 Hz with AC voltage of 5 mV.

The nature of the occurring paramagnetic structural point defects was assessed by low temperature (7-40 K) and room temperature (300 K) EPR spectroscopy. EPR data was recorded on a Bruker EMX Plus X-band (~ 9.43 GHz) EPR Spectrometer, equipped with a high sensitivity probe head. A ColdEdge™ ER 4112HV In-cavity Cryo-Free VT system connected with an Oxford temperature controller was used for low temperature measurements at 7 K. The Complete system was operated by Bruker Xenon software.

Chapter 3: Structural and Morphological Characterizations

Section 1 – XRD

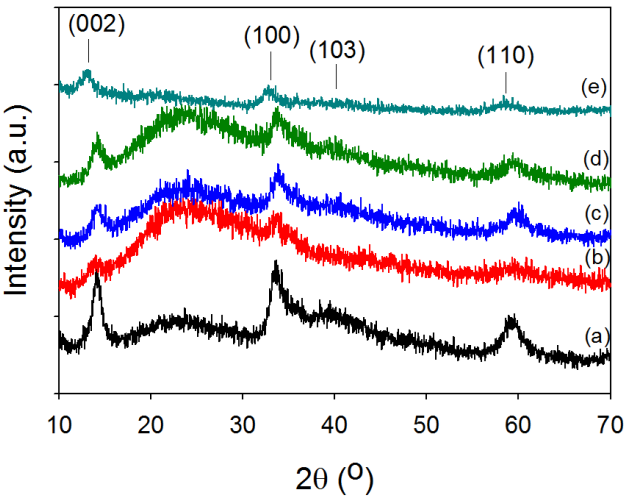

Figure 1: XRD pattern of (a) MoS_2, (b) $CoMoS_2$, (c) $NiMoS_2$, (d) $MnMoS_2$ and (e) $FeMoS_2$ with four distinguishable peaks for the planes (002), (100), (103) and (110)

To verify the crystal structure of our MoS_2 and doped MoS_2 samples, XRD was employed. Figure 1 shows the powder XRD pattern of the (a) MoS_2 nanostructures that can be indexed to hexagonal 2H-MoS_2 (JCPDS 37-1492) [16]. Four main peaks, seen in Fig. 1 are observed at 14, 33, 39, and 59 degrees corresponding to the (002), (100), (103) and (110) planes for MoS_2 respectively [25, 26]. The broad peak at 25 degrees comes from the glass substrate used to perform the measurements. Ojha *et al* presented [27] a similar XRD pattern for MoS_2 synthesized hydrothermally. The peak broadening is thought to come from better nanocrystalline nature of MoS_2 NCs. While Fig. 1 (b-e) of the doped MoS_2 samples show a decrease in intensity and broadening in the peaks, similarly seen in the study performed by Yoosuk [28]. Dai *et al* showed that doping MoS_2 with Co, without annealing, caused the XRD peaks to broaden [15]. This is thought to be due to $CoMoS_2$ having a more amorphous structure. Additionally, cobalt and nickel may be present in distinct phases, such as Co_9S_8 [29] and Ni_3S_4 located at ~30 and ~42 degrees. This means, after doping with the TMs, Co_9S_8 and Ni_3S_4 were not formed in the material. Additionally, upon doping with TMs, the hexagonal crystal structure is retained.

The Scherrer formula, $D_{hkl} = \frac{k\lambda}{\beta_{hkl} cos\theta}$, was used used to estimate the crystalline size of the MoS_2 nanostructures. Here, k is a coefficient (k = 0.9), β_{hkl} is the full-width-at-half maximum of the (002) peak, and λ is the wavelength (λ = 1.5405 Å). The calculated crystalline size from XRD line broadening is of 10 nm.

Section 2 – TEM

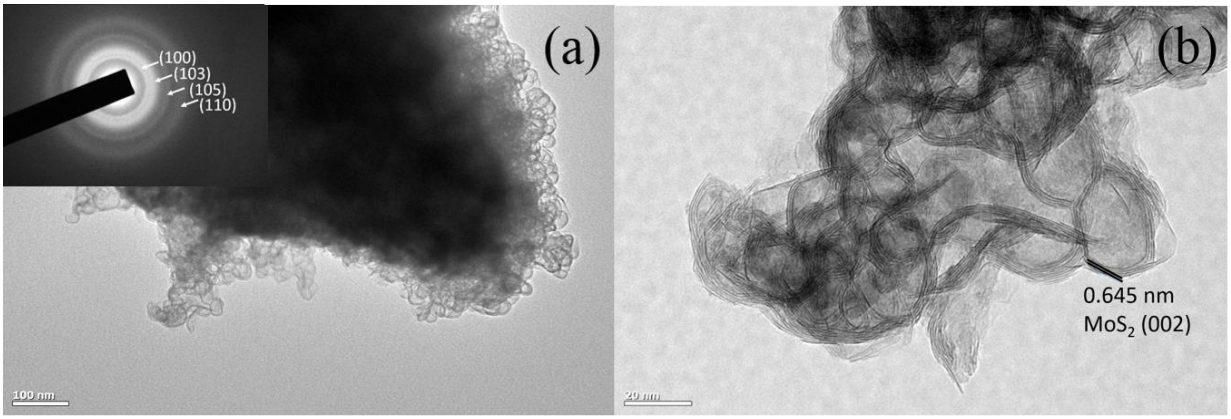

Figure 2: (a) Bright field transmission electron microscopic (TEM) image of MoS_2 nanocrystallites. The inset shows the SAED patterns confirming the nanocrystalline nature of the material. (b) High resolution electron microscope (HREM) image of MoS_2 nanocrystallites. The spacing between the layers along the (002) plane is about 0.645 nm.

Morphological studies were conducted using TEM. Figure 2 (a, b) shows the low magnification bright field and the high resolution lattice images, respectively. The selected area diffraction pattern (SAED) is shown as inset to the bright field image. As seen in Fig. 2(b), the MoS_2 nanocrystallites (of size, 25-30 nm) show the hexagonal structures made up of a few layers of MoS_2 basal planes. The apparent difference in the sizes estimated from Scherrer equation and TEM images might be because the Scherrer equation is an estimate of the crystallite size whereas the TEM image is a better approximation of the grain size. The SAED pattern shown as inset to Fig. 2(a) containing rings with uniform intensity all around confirm the nanocrystalline nature of the material. The interlayer spacing measured from the lattice images is 6.45 Å, consistent with the previous reports [30-35] (6.3 Å) of monolayer MoS_2 grown by the CVD methods and it

corresponds to the (002) planes of MoS_2. Additional measurements must be performed to estimate the spacing between the other planes, ex; (100), (001) and the (103) planes.

Additional TEM studies have shown the indication of doping Co and Ni into MoS_2 NCs. In the case of MoS_2 NCs, as shown in Fig. 3, only a few layers of MoS_2 are seen, whereas the Co and Ni doped MoS_2 NCs, seen in Fig. 4(a, b), show many thicker crystals with increased number

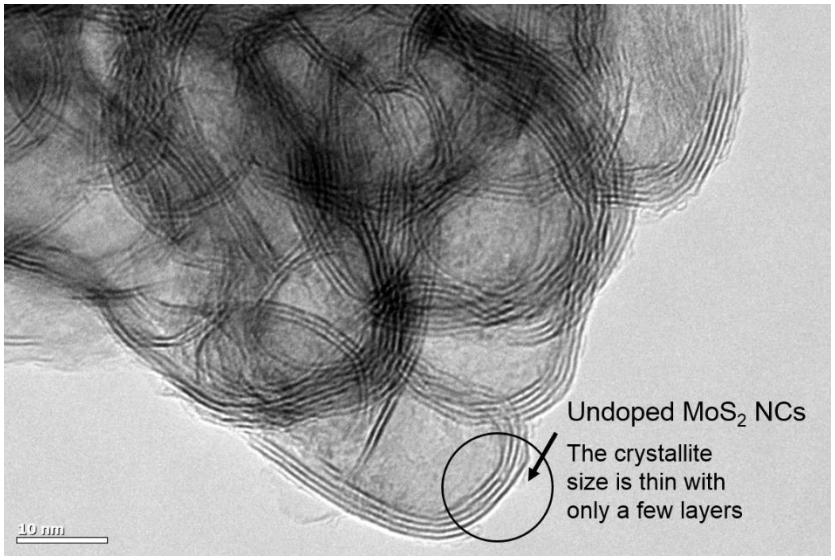

Figure 3: TEM image of MoS_2 NCs showing how the crystallite size is thin, containing few layers

of layers. Another observation that was noticed is that the undoped MoS_2 NCs show lattice fringes that are continuous without much break, but the doped samples show lots of breaks, bends and buckling. A similar observation has been reported previously by Xiang *et al* [36]. This indicates an increase in lattice defects/strain with doping.

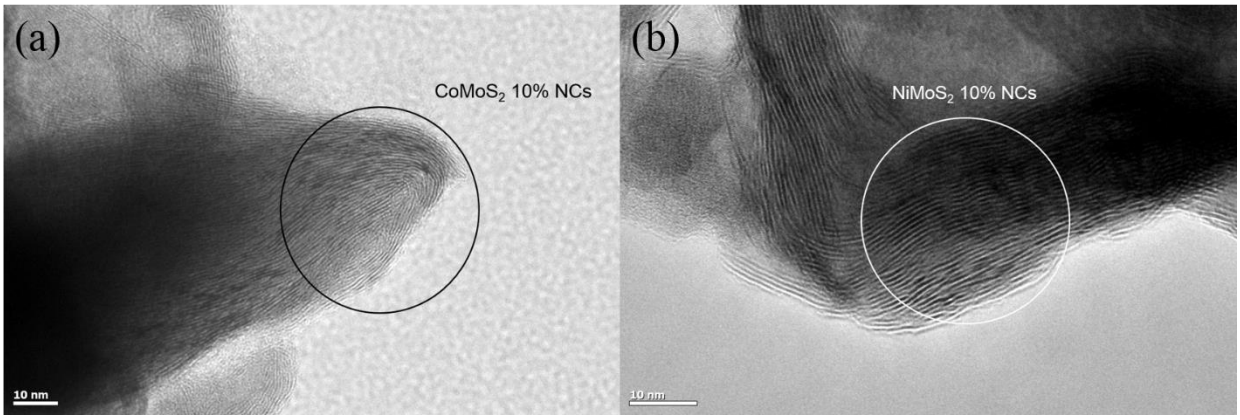

Figure 4: TEM images of (a) $CoMoS_2$ 10% NCs and (b) $NiMoS_2$ 10% NCs. Both show an increase in number of layers with bands, breaks and buckles.

Section 3 – RAMAN

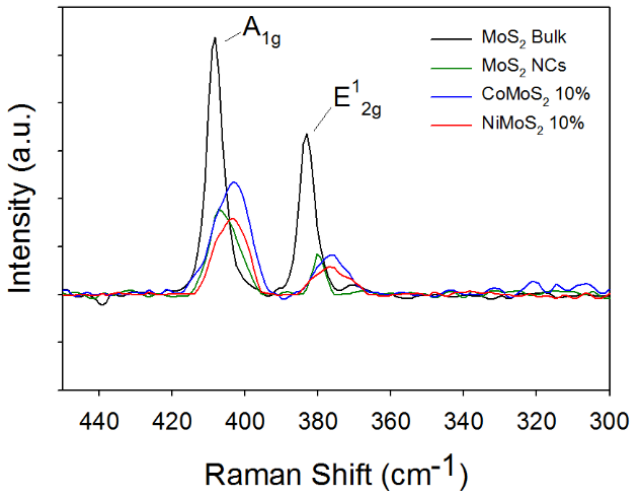

Figure 5: Raman spectra collected from MoS_2 bulk, MoS_2 NCs, $CoMoS_2$ and $NiMoS_2$. A slight blue shift was noticed for the MoS_2 NCs and for the doped samples.

Raman spectroscopy was used to confirm the few layered MoS_2, $CoMoS_2$ and $NiMoS_2$ NCs. Raman spectra measured on all of our samples showed two distinct characteristic peaks (as seen in Fig. 5) at 384 and 408 cm^{-1}, which are associated with the in-plane (E^1_{2g}) and out-of-plane (A_{1g}) vibrational modes of Mo-S bonds in 2H-MoS_2, respectively [27]. For the $CoMoS_2$ and $NiMoS_2$ Raman spectra, the frequency of the two vibrational modes decreases (376 and 403 cm^{-1}, respectively). The Raman peaks, for the pristine and doped samples, are in agreement with that of MoS_2 bulk crystals.

Section 4 – XPS

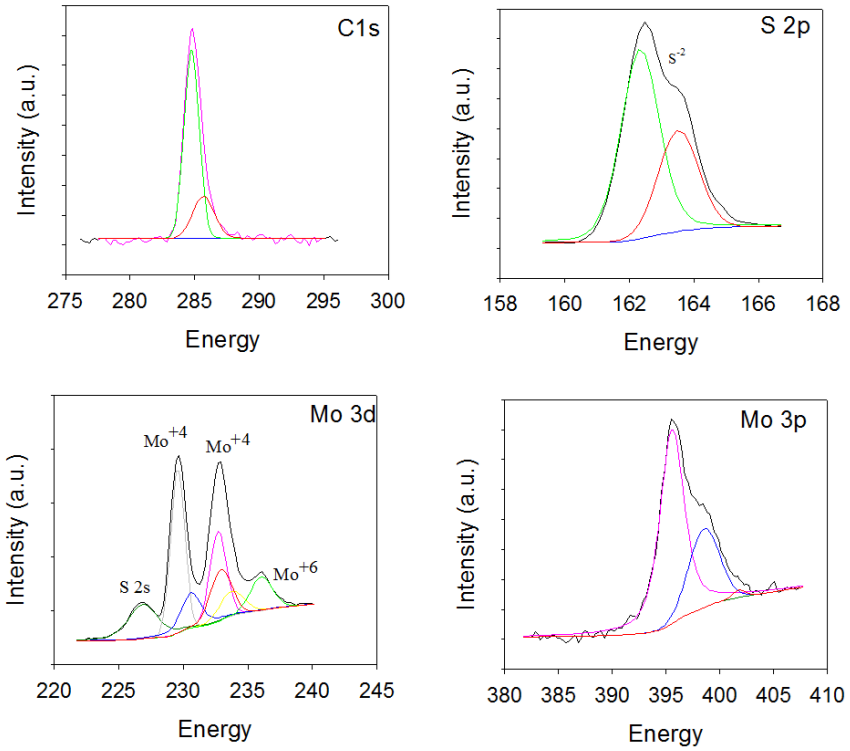

Figure 6: Core-level of Mo 3d, C 1s, Mo 3p and S 2p regions from MoS_2 nanocrystals. Core-level spectra of Mo 3d region has a predominant spin-orbit doublet (Mo $3d_{5/2}$ and Mo $3d_{3/2}$, $\Delta = 3.13$ eV) along with corresponding S 2p region spin-orbit doublet ($\Delta = 1.18$ eV). A secondary peak with a corresponding S 2p doublet on the higher binding energy is associated with the MoS_3 phase. A third Mo 3d peak at higher binding energy with an associated O 1s peak (see Figure 7) corresponds to Mo (VI) O_3.

XPS survey spectra of MoS_2 NCs indicate the presence of peaks with binding energies (BE) consistent with molybdenum and sulfur elements besides a lower intensity oxygen and carbon. Absence of other elements demonstrates the purity of the sample. To further probe the chemical composition and surface chemistry, high-resolution core-level XPS spectra were collected on the selected BE intervals. The BE positions were referenced and adjusted to adventitious carbon because of the charging effects on the sample. Shirley method background signal was subtracted and BE peaks were curve-fitted (deconvolution) using Gaussian/Lorentzian functions. Multiple binding energies associated with C 1s spectra are observed at 284.4 eV, 286.3 eV and 287.9 eV, as seen in Fig. 6, which are assigned to adventitious carbon and C-O impurities from hydrothermal process. O 1s spectral region peak at 532.6 eV resulting from C-O bonding while the lower BE peak 530.8 eV is ascribed to Mo-O bonding, seen in Fig. 7. The deconvoluted Mo 3d region had multiple peaks at 228.9 (Mo $3d_{5/2}$), 229.9 (Mo $3d_{5/2}$), 232.48(Mo $3d_{5/2}$) and its corresponding spin-

orbit splitting doublet peaks appearing at 232.08 (Mo $3d_{3/2}$), 233.1 (Mo $3d_{3/2}$), 235.6 (Mo $3d_{3/2}$) respectively, along with S 2s peak showing up at 226.3 eV. Spin-orbit split peak separation is found to be around 3.16 eV, which is consistent with the existing literature [37 - 39]. The peaks, corresponding to the S $2p_{3/2}$ and S $2p_{1/2}$ orbital of divalent sulfide ions (S^{2-}), are observed at 161.8 and 162.98 eV with another set of deconvoluted peaks appearing at 163.6 eV and 164.8 eV with an estimated spin-orbit splitting of 1.18 eV. Multiple BE peaks observed in this sample are apparently indicating different phases. The high intensity peak at 228.9 eV (Mo $3d_{5/2}$) resulting from Mo^{4+} oxidation state is ascribed to MoS_2 phase [37]. Further, the BE peak at 232.48 eV (Mo $3d_{5/2}$) relating to higher oxidation state of Mo^{6+}, in conjunction with O 1s, (530.8 eV) is attributed to a mostly stable MoO_3 phase [39]. The XPS technique can also be used to quantify the ratio of different phases within a given sample. Based on the deconvoluted Mo3d peaks, it is estimated that there is about 65% MoS_2 phase and the remaining is a combination of MoS_3 and MoO_3. XPS spectra collected on MoS_2 bulk crystals showed characteristic features, without any residual phases.

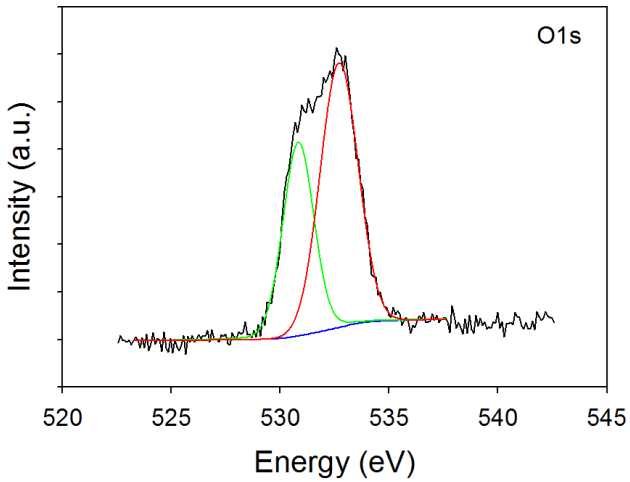

Figure 7: Core-level of O 1s region corresponding to the high binding energy peaks in Mo 3d in Figure 4.

To verify whether Co and Ni were doped into MoS_2 NCs additional XPS measurements were performed and studied in collaboration with Prof. Lopez's group in UTEP Physics. The presented results of the electronic ions structure are related to the binding energies found for molybdenum (Mo^{42}), sulfur (S^{16}), nickel (Ni^{28}) and cobalt (Co^{27}). Figure 8(a, c and e) show the XPS BE for (Mo) 3d-orbital from ~234 to 225 eV, respectively. The BEs were found at 230.1 and

226.9 eV for pure MoS_2. The BE's for the Mo 3d-orbital in $NiMoS_2$ were found at 230.7 (Mo 3d3/2) and 227.5 eV (Mo 3d5/2). The Mo 3d orbital Binding energies for $CoMoS_2$ were found at 229.9 (Mo $3d_{3/2}$) and 226.8 eV (Mo $3d_{5/2}$), where a clear horizontal shift can be seen for the $CoMoS_2$ Mo 3d orbital. The explanation is that Mo $3d_{5/2}$ orbital is linked to the S 2s orbital in MoS_2, which is linked to Ni in the form of Ni-(MoS_2). For the cobalt case, the Mo $3d_{5/2}$ orbital is linked to the S 2s which is also linked to cobalt (II) tetrathiomolybdate (III) in Co-Mo_2S_4. The Mo $3d_{3/2}$ orbital is linked to MoO_3 in MoS_2, which is also linked to Ni-Mo and Co-Mo, respectively [40-48]. The absence of extra peaks within the Mo 3d spectra points to a relatively small amount of MoO_3 in all three samples. Fig. 8(b) shows the spectrum between 170 and 150 eV which contains well-formed signals at 160.2, 160.8 and 160.2 eV. These are related to the S 2p orbital in MoS_2 (S/Mo), $NiMoS_2$ (in the form NiS and S/Ni) and $CoMoS_2$ (CoS), respectively [49-52, 49, 53]. Fig. 8(d) shows a well-defined peak at 852.6 eV with a FWHM of 3.3 eV corresponding to the Ni 3p-orbital in $NiMoS_2$ [54, 55]. The peak at this location is the best indicator of successful nickel doping [56]. Fig. 8(f) shows the Co 3s orbital spectrum which contains two signals at 102.2 eV and 100.1 eV, and can be attributed to CoS_2 and to the Co 3s orbital, respectively [57,58].

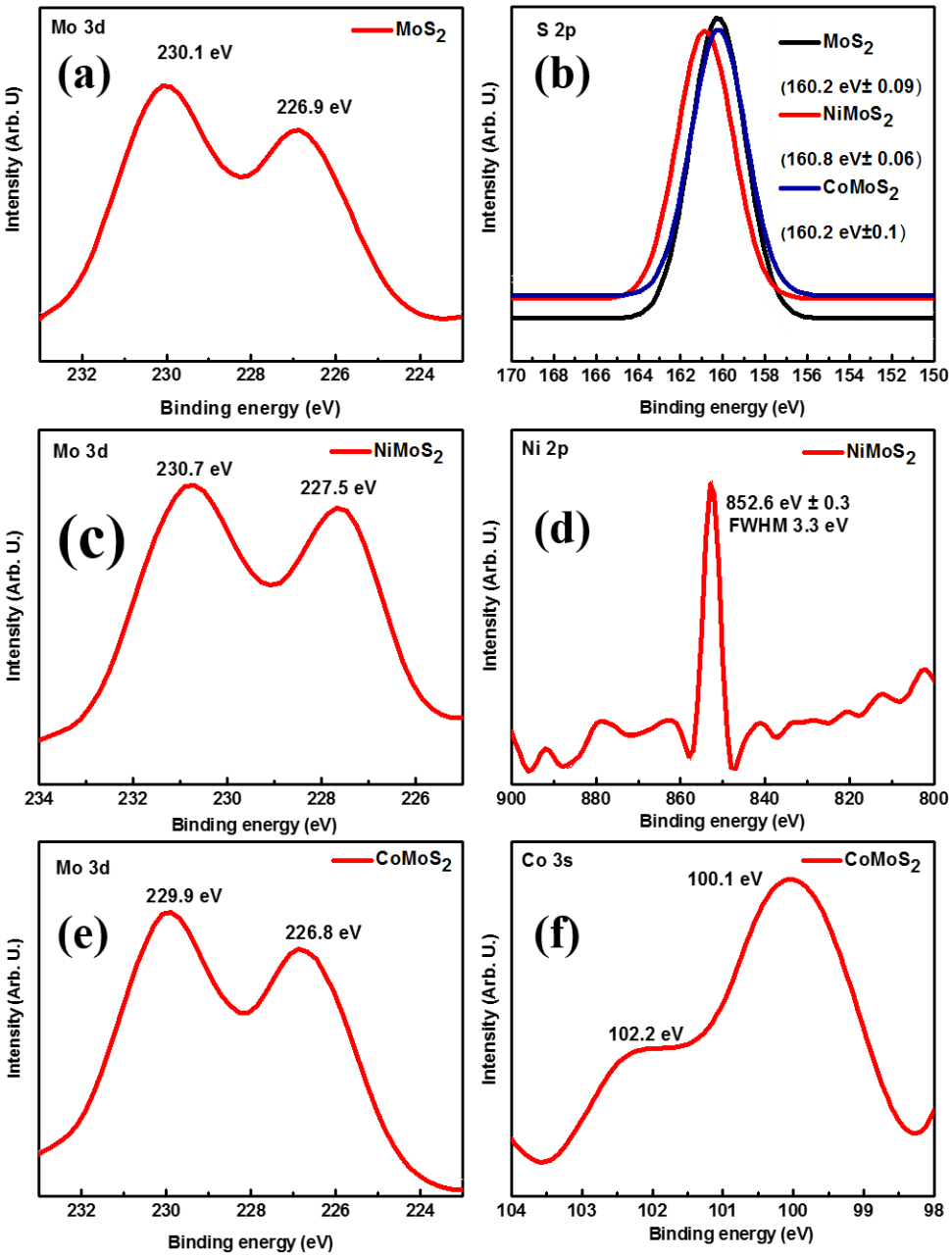

Figure 8: XPS signals of (a) MoS_2, Mo $3d_{5/2}$ and Mo $3d_{3/2}$ regions, (b) S 2p region of MoS_2, $NiMoS_2$ and $CoMoS_2$, (c) $NiMoS_2$, Mo $3d_{5/2}$ and Mo $3d_{3/2}$ region, (d) Ni 2p region, (e) $CoMoS_2$, Mo $3d_{5/2}$ and Mo $3d_{3/2}$ region, and (f) Co 3s region.

Chapter 4: Magnetic Characterization

Section 1 – MoS_2 NCs

To study the magnetic properties of MoS_2 NCs, temperature- and magnetic field-dependent magnetization measurements were performed [16 - 17]. In Fig. 9(a) the temperature dependent magnetization can be observed. The magnetization was measured from 10 – 300 K, after a $\mu_0 H$ = 1 T magnetic field cooling. As it can be noticed, the magnetization increased with cooling. A similar observation was reported on many other materials [60 - 63] such as exfoliated WS_2 nanosheets, graphene nanoribbons, Li intercalated MoS_2 nanosheets, and amorphous MoS_2.

To better understand the observed magnetic behavior, the χ-T curve was fitted using the modified Curie-Weiss (CW) model [61] $\chi = \chi_{DM} + \frac{C}{(T+\theta)}$, which involves the diamagnetic and paramagnetic contributions. Here χ_{DM} is the diamagnetic susceptibility, C = Curie constant, θ = CW temperature, and T = measurement temperature. Here the paramagnetic component is used as $\chi_{PM} = \frac{C}{(T+\theta)}$, where + θ indicates antiferromagnetism and – θ indicates ferromagnetism. The fitting results (blue) are shown in Fig. 9 (a) along with the experimental data (black).

Table I: Values obtained from modified CW model

Sample	**C**	**θ (K)**	**χ_{dm}**
Undoped MoS_2 NCs	4.764e-04	3.406	-9.454e-07
Fe doped MoS_2 NCs	4.257e-04	3.296	-3.732e-07
Ni doped MoS_2 NCs	5.396e-04	3.173	-6.123e-07
Co doped MoS_2 NCs	9.895e-04	2.935	1.883e-06
Mn doped MoS_2 NCs	3.756e-03	2.841	-5.526e-06

Both the diamagnetic and paramagnetic components are resolved. In addition, the fitting results are tabulated in Table I. The obtained value of θ was 3 K for the MoS_2 NCs. As shown in Table I, the value of θ is positive indicating antiferromagnetic behavior, which, however, is associated with uncompensated spins that result in finite magnetization. That is the typical signature of canted antiferromagnetic phase. Negative θ values would indicate ferromagnetism.

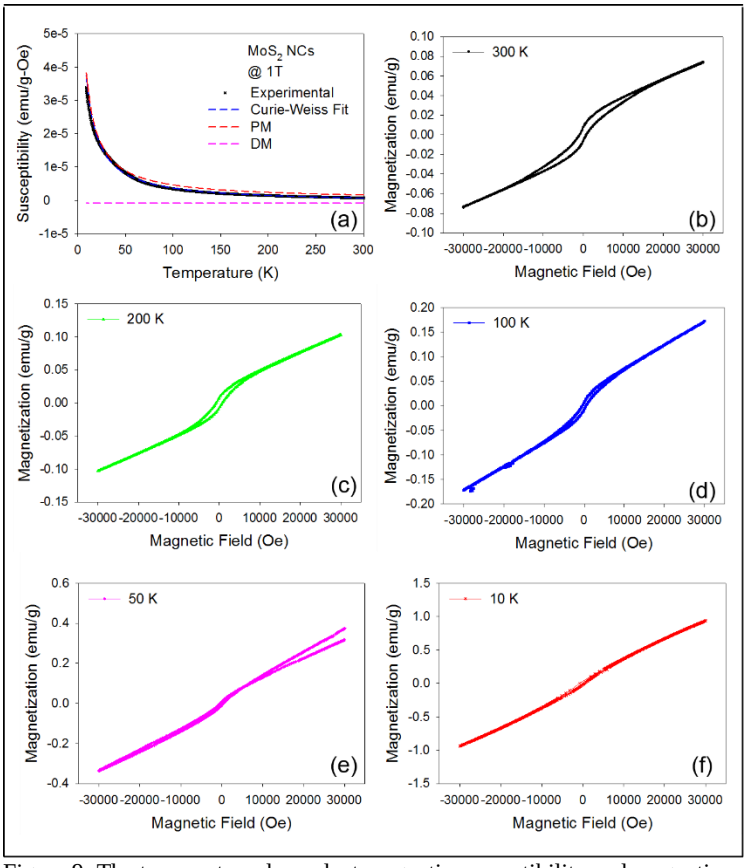

Figure 9: The temperature dependent magnetic susceptibility and magnetic field-dependent magnetic behavior of MoS2 NCs. Fig. 6(a) also includes the applicability of modified Curie-Weiss model.

Now, our attention turns to the magnetic field dependent magnetization behavior. Isothermal magnetization as a function of magnetic field were measured between 10 and 300 K. The data is plotted in Fig. 9(b-f). At 10 K, observations of a nearly anhysteretic behavior with positive slope indicates canted antiferromagnetic phase. As temperature increases further, a more magnetic hysteresis behavior was observed at low fields but the anhysteretic behavior persists at higher fields. These features together with M-T variation (Fig. 9(a)) indicates that MoS_2 NCs showed a canted antiferromagnetism at low temperature and ferromagnetism at room temperature. Verifying with the modified Brillouin function [61] (see below) could not account for the 100 K M-H behavior, as seen in Fig. 10.

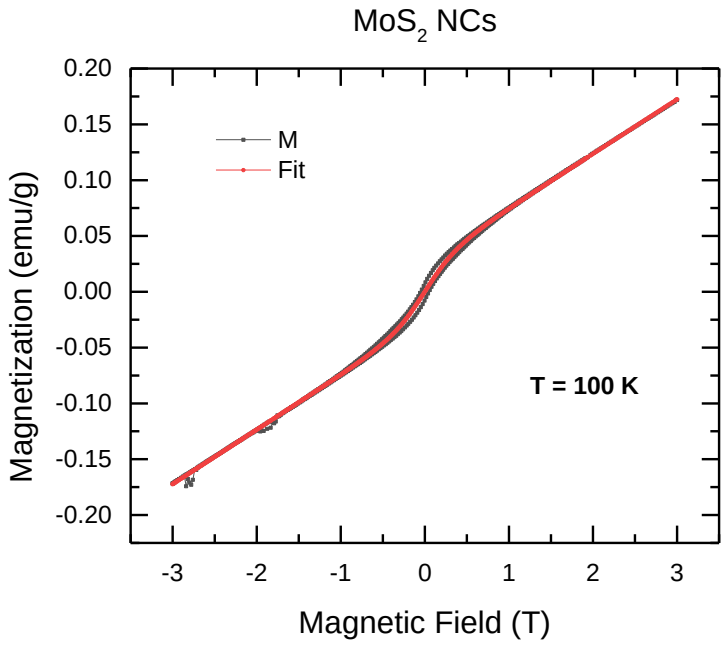

Figure 10: Magnetization vs Magnetic Field curve for pristine MoS_2 NCs with the modified Brillouin fit.

$$M = X_d H + Ms[\frac{2J+1}{2J}\coth\left(\frac{2J+1}{2J}X\right) - \frac{1}{2J}\coth\left(\frac{X}{2J}\right)]$$

This function consists of a linearly field dependent function, which represents diamagnetism added with the classic Brillouin function, which refers to paramagnetism. In the above equation, the variable M_S is the saturated magnetization $Ms = Ng\mu J$, where N is the density of spins, μ is Bohr's magneton, g is the Lande g-factor, and J is the angular momentum number. The variable X is equaled to X = $gJ\mu H/kT$, where k is Boltzmann's constant, and T is temperature. By using the modified Brillouin function, the fits were obtained for the accumulated data. However, the numerical values of temperature in our fits did not correlate with what was seen in experimentation, verifying that the modified function could not account for the magnetic-field dependent magnetization data that was observed at 100 K. A strong hysteretic behavior was noticed at 300 K rather than at 10 K. This observation is also reflected in the temperature dependent coercive field (H_C) trend plotted in Figure 11. It was noticed that the H_C increased from 373 to 880 Oe as the

temperature increased from 10 to 300 K. This infers that the ferromagnetism observed at room temperature is of short-range.

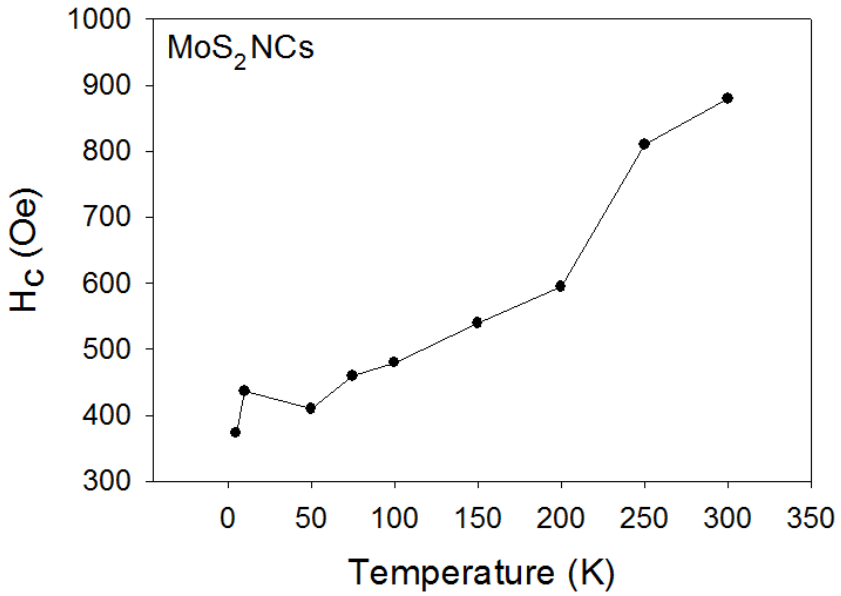

Figure 11: The temperature variation of the coercive field of MoS_2 NCs

To corroborate the magnetic data, the temperature dependent (50-300 K) resistance measurements (data not shown) were performed on all the materials studied here, including undoped MoS_2 NCs. The data showed semiconducting behavior (resistance increases as the sample is cooled), consistent with the literature reports [64], and revealed very little (<0.5%) magnetic field dependence even upon the application of 3 T magnetic field. These observations are typical of canted antiferromagnetism. In the sections below, the magnetic and catalytic properties of doped MoS_2 NCs is discussed.

Section 2 – $CoMoS_2$ NCs

The temperature dependent magnetic susceptibility (χ - T) data was collected after the sample was cooled to 10 K in $\mu_0 H$ = 1 T magnetic field (see Fig. 12(a)). The magnetization value (0.8 emu/g) observed in the present study is higher than those (0.006 to 0.3 emu/g) reported [65, 62, 66, 67] in the literature on similar systems such as Co, Cu, and V doped (<7% doping) MoS_2 nanostructures prepared through hydrothermal method.

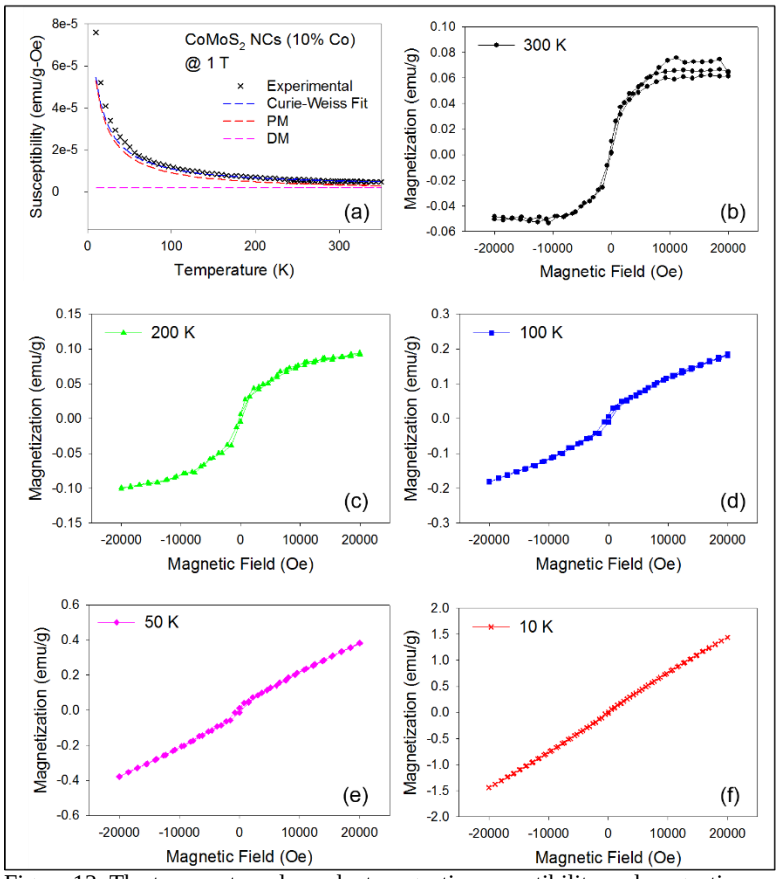

Figure 12: The temperature dependent magnetic susceptibility and magnetic field-dependent magnetic behavior of Co doped (10%) MoS_2 NCs. Fig. 8(a) shows the applicability of modified Curie-Weiss model.

As displayed in Fig. 12(a), the modified CW model describes well the temperature dependent magnetic susceptibility behavior. A positive θ_{CW} of 3 K (see Table I) was obtained which indicates that the material is antiferromagnetic below the temperature of 3 K.

Isothermal magnetization measurements were performed on Co doped MoS_2 NCs by sweeping the magnetic field from -2 to +2 T at various temperatures (10, 50, 100, 200 and 300 K). The data is presented in Fig. 12 (b-f). At 10 K, magnetization shows anhysteretic behavior with the magnetic field with the positive slope, which indicates the (canted) antiferromagnetic behavior. Interestingly, with further increase in temperature, a more hysteretic behavior with coercive field of 400 Oe becomes pronounced, suggesting unambiguous room-temperature ferromagnetism, as evidenced from the s-shaped hysteresis loop. In addition, the Brillouin function could not account for the magnetic field dependent magnetization data observed at 100 K due to a mismatch with the temperature given back by the function. The saturation magnetization (magnetization at the maximum applied magnetic field) decreases as the measurement temperature increases from 10 – 300 K. This trend is consistent with the temperature

dependent magnetic susceptibility data as shown in Fig. 12(a). Xiang and co-authors have also reported [65] room temperature ferromagnetism from Co doped (<7%) MoS2 nanosheets.

The XRD patterns (Fig. 1) obtained on the samples studied here are identical to the ones reported on the best samples prepared through hydrothermal method in the literature [60, 65, 62, 68] thus confirming that there is no or minimal segregation/clustering of dopants. If there is a significant clustering effect, one would expect to observe higher ferromagnetic Curie temperature beyond room temperature [69], which is clearly not the case here.

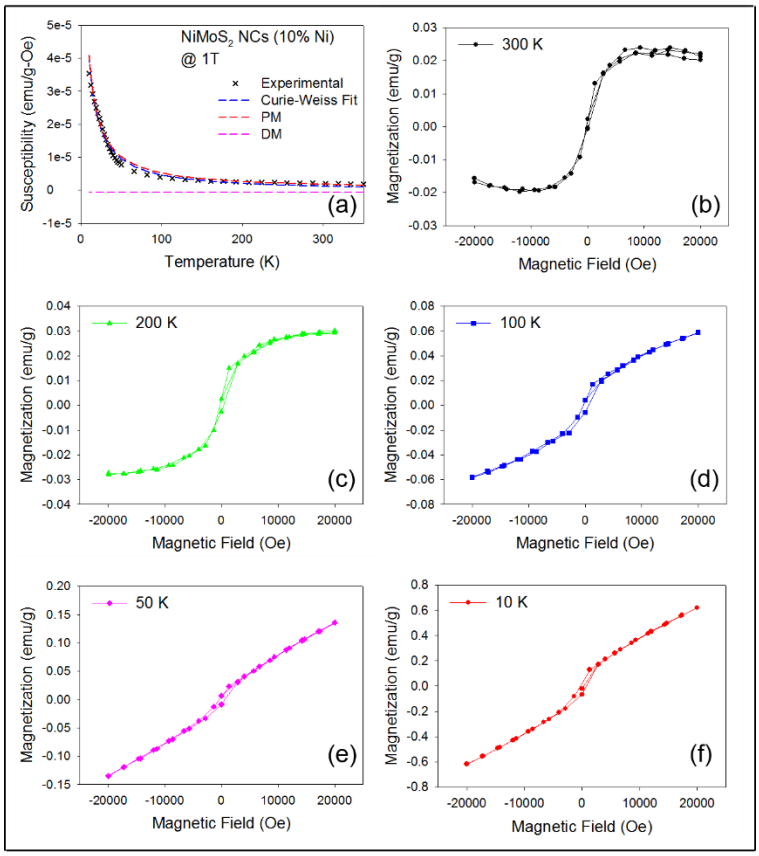

Figure 13: The temperature dependent magnetic susceptibility and magnetic field-dependent magnetic behavior of Ni doped (10%) MoS2 NCs. Fig. 9(a) shows the applicability of modified Curie-Weiss model.

Section 3 – $NiMoS_2$ NCs

Similarly, the temperature dependent magnetic susceptibility data, for $NiMoS_2$ NCs, was collected after the sample was field cooled at $\mu_0 H$ = 1 T magnetic field (Fig. 13(a)). The magnetization values (0.4 emu/g) observed in this study are comparable to those reported in the literature on similar systems [65, 62, 66, 67]. The modified CW model, as depicted in Fig. 13(a) can describe well the temperature dependent magnetization behavior giving a θ_{CW} = 3 K, as seen in Table I.

Isothermal magnetization measurements have been performed on Ni doped MoS_2 NCs by sweeping the magnetic field from -2 to +2 T at various temperatures (10, 50, 100, 200 and 300 K), as seen in the data presented in Fig. 13 (b-f). At 10 K, magnetization anhysteretic behavior as a function of magnetic field was observed, which indicates (canted) antiferromagnetic behavior. Interestingly, as the temperature starts to increase further, an s-like hysteresis associated with the coercive field of 175 Oe, suggesting unambiguous room temperature ferromagnetism. The saturation magnetization decreases as the measurement increased from 10-300 K. This trend is consistent with the temperature dependent magnetic susceptibility data shown in Fig. 13(a). Similar to the $CoMoS_2$ NCs case, Brillouin function could not account for the magnetic field-dependent magnetization observed at room temperature. To our knowledge, with the exception of one report [69] on the catalytic behavior of Ni doped MoS_2 nanoparticles, there have been no previous works reported on the magnetic properties of Ni doped MoS_2 NCs, to compare our data at any doping percentage.

Section 4 – $FeMoS_2$ NCs

Like the measurements performed on Co and Ni doped MoS_2 NCs, magnetization data on Fe doped MoS_2 NCs has been collected. The temperature dependent magnetic susceptibility data was collected after the sample was cooled in $\mu_0 H$ = 1 T magnetic field (see Fig. 14(a)). The magnetization value (0.3 emu/g) obtained from the χ-T curve is comparable to that (0.25 emu/g) reported in the literature on Fe doped (1.74%) MoS_2 nanostructures [68]. As displayed in Fig. 14(a), the modified CW model describes well the temperature dependent magnetic susceptibility behavior with a θ_{CW} = 3 K (see Table I).

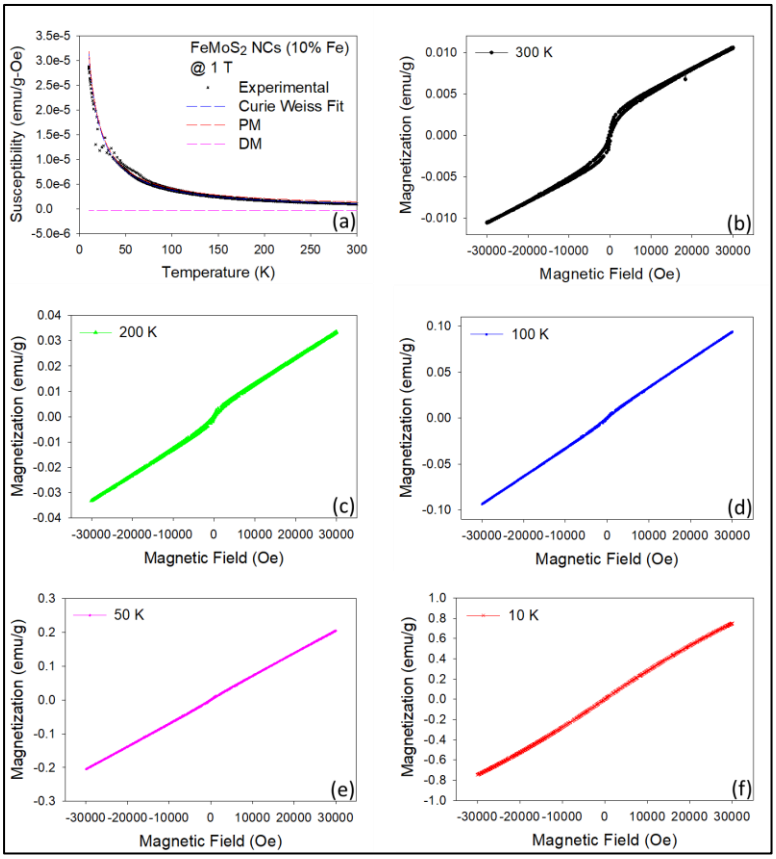

Figure 14: The temperature dependent magnetic susceptibility and magnetic field-dependent magnetic behavior of Fe doped (10%) MoS2 NCs. Fig. 10(a) shows the applicability of modified Curie-Weiss model.

The isothermal magnetization data is presented in Fig. 14 (b-f). At 10 K, similar to the previous samples, magnetization shows anhysteretic behavior with the magnetic field, which indicates (canted) antiferromagnetic behavior. However, at 300 K, the M-H behavior of this material shows a combination of ferromagnetic (at low fields) and antiferromagnetic behavior (at high fields). This is in sharp contrast with Co and Ni doped samples, which show complete ferromagnetic behavior at room temperature. The saturation magnetization decreases as the measurement temperature increased from 10-300 K. This trend is consistent with the temperature dependent magnetic susceptibility data shown in Fig. 14(a). In addition, the Brillouin function could not account for the magnetic field-dependent magnetization data observed at room temperature. Xia and co-authors also reported [68] room temperature ferromagnetism in Fe doped (<3.18%) MoS_2 nanosheets prepared through the hydrothermal process. The interaction between the sulfur vacancies and the dopants is argued to be at play. A similar situation may be expected to happen in the present case as well.

Section 5 – $MnMoS_2$ NCs

Temperature dependent magnetic susceptibility and magnetic field dependent magnetization measurements were performed on Mn doped MoS_2 NCs. As shown in Fig. 15(a), the magnetic susceptibility increased as the sample temperature is lowered from 300 to 10 K. More importantly, the magnetization measured at 10 K (1 T), is about 6-times higher than that of pure MoS_2 NCs (Fig. 9(a)). This observation is the direct effect of doping with Mn. To gain additional insights into the magnetism, the χ-T curve was fitted using CW model comprising of diamagnetic and paramagnetic contributions. The highest Curie constant of 4×10^{-3} obtained from the χ-T curve fitting signifies the larger magnetization in comparison to the materials discussed above. The fitting results are shown in Fig. 15(a) along with the experimental data. By following this model, the diamagnetic and paramagnetic components and CW constant was obtained (see Table I), which indicates that the material is antiferromagnetic below 3 K. However, a much weaker ferromagnetism was observed at 300 K as reflected from the hysteretic behavior at low fields, and a predominant paramagnetic nature was observed at higher fields, shown in Fig. 15 (b-e). A similar weak ferromagnetism was previously reported [71] for Mn doped SnSe alloys prepared via

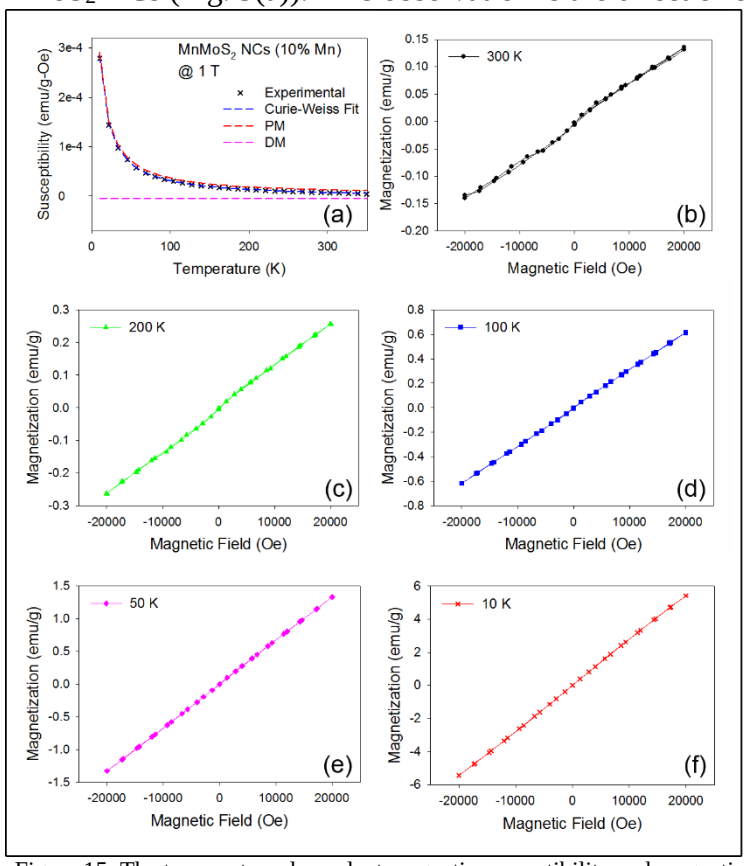

Figure 15: The temperature dependent magnetic susceptibility and magnetic field-dependent magnetic behavior of Mn doped (10%) MoS2 NCs. Inset of Fig. 11(a) shows the applicability of modified Curie-Weiss model.

molecular beam epitaxy methods. Wang and co-workers reported [62] room temperature ferromagnetism in Mn doped (7%) MoS_2 NCs. Park and co-authors have reported [72] a similar room temperature ferromagnetism from MoS_2 NCs upon doping with MnO_2 by electrochemical method, associated with the saturation magnetization of 0.02 emu/g.

MoS_2 has been shown, in the literature, to contain ferromagnetism from the zig-zag edges or vacancies of the material [16 - 17], which could be a similar case here. Our MoS_2 NCs are seen to contain various paramagnetic defects, including sulfur vacancies (as seen in Chapter 6) which could be responsible for the ferromagnetism observed here. This work also shows that magnetic properties can strongly depend on the nature of the dopant as well. Additionally, the magnetic order-disorder transition varies with dopant type such as Co and Ni doping produces stronger ferromagnetic behavior than Fe and Mn at least at 300 K.

Chapter 5: Electrocatalytic Characterizations

It has been shown that the electrocatalytic performance of MoS_2 NCs can be engineered by doping the active edge sites with transition metals. To study HER performance, polarization curves (see Fig. 16) were obtained for MoS_2 NCs and the doped samples. At an overpotential (η) of 300 mV, the current densities for MoS_2, $CoMoS_2$, $NiMoS_2$, $FeMoS_2$ and $MnMoS_2$ were found

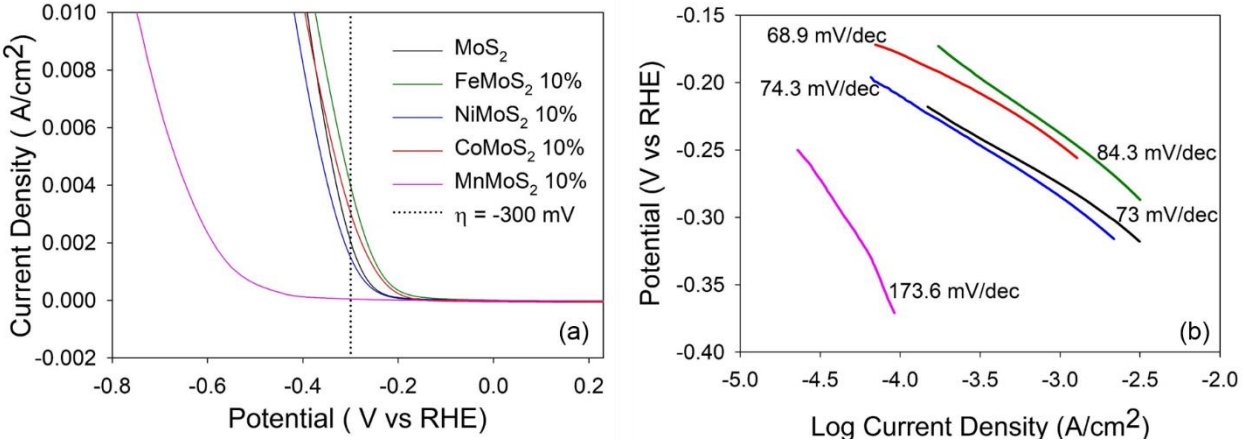

Figure 16: (a) Polarization curves, (b) Tafel plots of pristine and 10% doped (Co, Ni, Fe, and Mn) MoS_2 NCs.

to be 2.09, 3.00, 1.5, 4.05 mA/cm^{-2} and 52 uA/cm^{-2}. Listed from greatest to least for comparison, the reaction kinetics are as follows: $FeMoS_2 > CoMoS_2 > MoS_2 > NiMoS_2 > MnMoS_2$; this was observed to be true for $-372.8\ mV \leq \eta \leq -169.6\ mV$. This progression is the exact same order of activity that was previously found by calculating the hydrogen absorption free energy (ΔG_H). Wang *et al* and other groups have doped different transition metals to MoS_2 nanostructures similar to the metals used here and observed current densities that are comparable with our data [13, 56, 73]. The onset potential for the MoS_2 NCs was 141 mV, which is comparable to the work done by X. Ren [74]. These observations are consistent with the literature reports.

For the HER, the Tafel slope and exchange current density can provide information about the reaction mechanism and kinetics of the process. The Tafel slopes also indicate the rate-limiting step in the HER [75]. Essentially, the lower the Tafel slope, the faster the reaction takes place, and

the faster hydrogen is produced. Doping with different transition metals showed a slight change in the Tafel slope, as seen in Fig. 16 (b), which is consistent with other literature reports [13, 56, 76, 77].

EIS was performed on the samples at overpotentials of 0.445, 0.5, 0.545, and 0.645 V. Figure 17 shows the EIS measurements taken at η = 0.5 V. Smaller semicircle diameters correspond to higher charge transfer, higher conductivity, and lower charge transfer resistance (R_{ct}). The samples can be ranked in order from least to greatest R_{ct} in the following order: Fe, Co, Pristine MoS_2, Ni, and Mn.

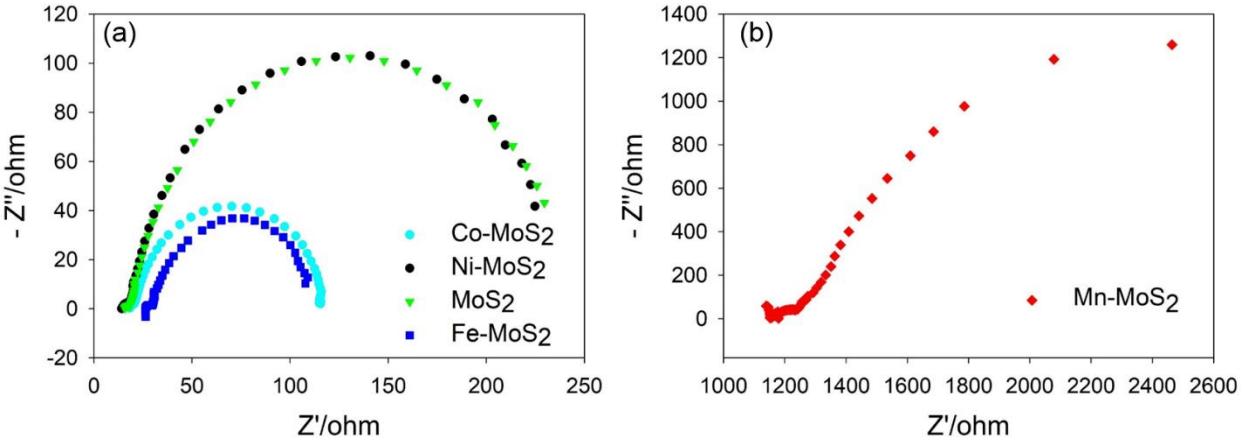

Figure 17: (a) EIS plots for Co, Ni, Fe doped MoS_2 NCs, and pristine MoS_2 NCs; η = 0.5 V. (b) EIS plot for Mn doped MoS_2 NCs; η = 0.5 V.

Fe doped MoS_2 NCs have the greatest conductivity and charge transfer ability, while Mn-doped MoS_2 NCs have the least. DFT calculations performed by Wang and co-authors [13] shows that the S-edges should become more active once they are doped with TMs. Their experimental findings have shown that the active sites double in activity when doped with Fe, Co and Cu. Another literature report performed a similar electrocatalytic study of TM-doped MoS_2 and found the exact same progression [13], with R_{ct} increasing from Fe to Ni in the same order. Our additional study (Figure 17 (b)) of Mn doped MoS_2 showed poor HER performance.

The electrocatalytic performance of $CoMoS_2$ NCs was examined using chronoamperometry to determine the long-term stability of the NCs. The chronoamperometric studies were operated in a custom-built two-compartment gas-tight electrochemical cell under an argon atmosphere. One of the compartments of the cell contains the counter electrode. The solution (0.5 M H_2SO_4 in water) was saturated with argon gas prior to the measurement and the solution in the side of the cell containing the working electrode was kept stirring to remove the in-situ generated hydrogen gas. The experiment was conducted with an initial current density of 10 mA/cm^2 along with a constant over potential of at $\eta = 850$ mV. The current density was observed

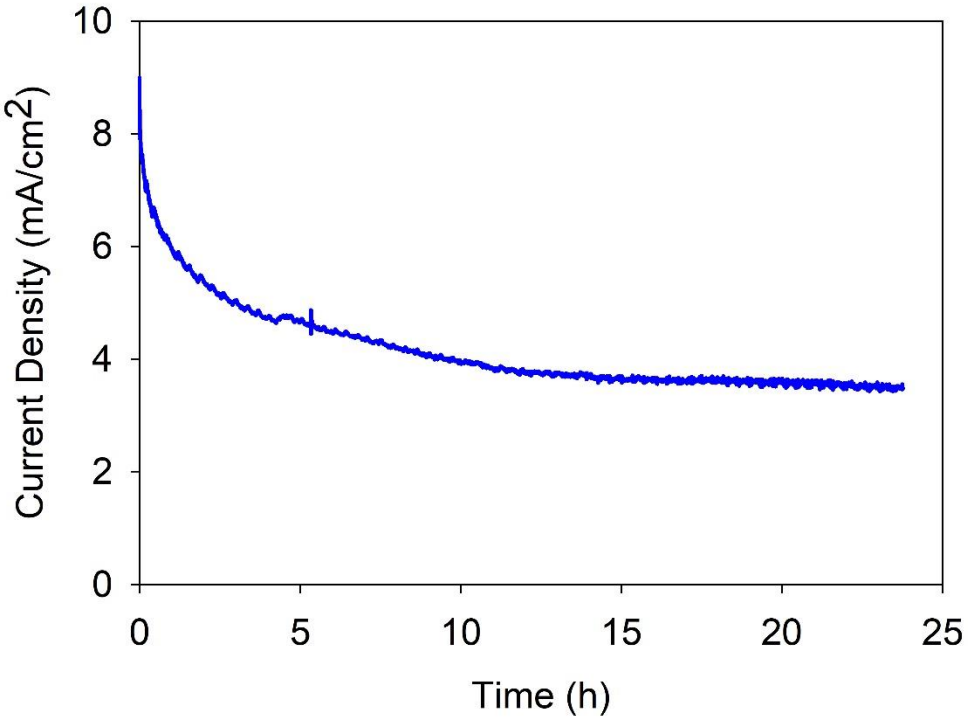

Figure 18: Stability test for $CoMoS_2$ performed at $\eta = 850$ mV

to stabilize after approximately 5 hours, and after over 23 hours of operation, the $CoMoS_2$ NC's can be seen to be electrocatalytically active. Thus, the stability of the nanocrystals has been demonstrated through pragmatic means.

Chapter 6: EPR Characterization

In the previous chapters, various characterization methods have been employed to study the material's structure, morphology, valence states, magnetic characteristics and catalytic activity. Yet, to truly complete this study a more profound look must be taken into this material. In this chapter, X-band (~9.4 GHz) EPR spectroscopy is used to identify atomic paramagnetic point defects. This, in turn, will help in finding a correlation between the catalytic activity and the paramagnetic centers.

Section 1 – MoS_2 NCs EPR

Initial EPR measurements were performed at 7 K to study the paramagnetic centers in MoS_2 NCs [23]. The data is shown in Fig. 19. Similar measurements were performed on MoS_2 bulk, which showed a completely distinct EPR spectra due to different extrinsic defects present within the sample. The spectrum exhibits a wealth of information pertaining to intrinsic paramagnetic spin centers. *To the knowledge of the author, this is the first single richest spectrum reported to date on any MoS_2 nanocrystalline, and amorphous/less-crystalline compounds.* EPR spectral parameters provide characteristic

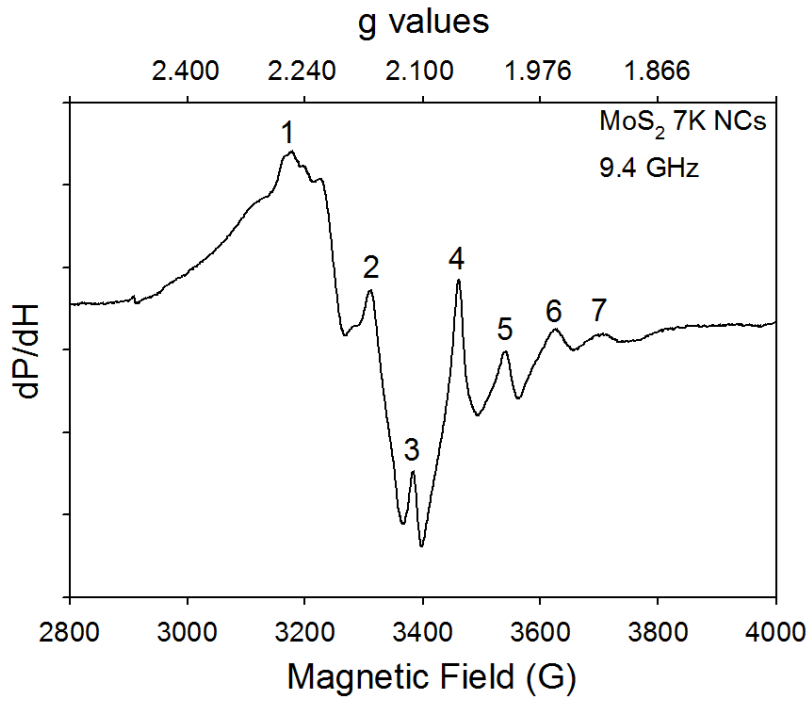

Figure 19: First-derivative representative X-band (9.40 GHz) EPR spectra measured on MoS_2 nanocrystals at 7 K. One can see that there are at least seven well-resolved EPR lines as marked from 1 to 7. The spectrum is plotted on both the magnetic field and g-value axes.

signatures of paramagnetic defects by analyzing the signal position, width, and shape. From this spectrum, at least seven well-resolved signals have been identified, marked from 1 to 7. Only those peaks that are clearly observable are indicated. Since the signals show considerable overlap, it is difficult to determine the EPR parameters of each signal accurately. Nevertheless, within experimental accuracy, the g-values of all the well-resolved peaks and their peak-to-peak line widths that could be detected separately are tabulated in Table II and Table III, respectively. The g-values were determined using the resonance condition $h\nu = g\beta H$ where h = Planck's constant, ν = microwave frequency, g = g-value, β = Bohr magneton, H = resonance field (measured at the turning points). Collected at 7 K, on as prepared MoS_2 nanocrystals, seven EPR signals, associated with g_1 = 2.114, g_2 = 2.030, g_3 = 1.986, g_4 = 1.941, g_5 = 1.898, g_6 = 1.854, and g_7 = 1.814 have been analyzed. No half-field lines were detected that might correspond to electron spin > ½. Most likely, the signals that are observed in this study arise form spin ½ paramagnetic spin centers. Though an intense search was performed, no trace of hyperfine interaction originating from ^{33}S (nuclear spin I = 3/2; 0.75% abundance) and, ^{95}Mo and ^{97}Mo (both I = 5/2; 25.5% added abundance). No external impurities were observed from MoS_2 nanocrystallites unlike in the bulk single crystals of 2H-MoS_2, from which in our group and other researchers [78-80] have observed unwanted Re, As, Pb, Fe and Ni. In addition, as verified from the controlled measurements, no similarity between the EPR spectra measured on MoS_2 nanocrystals and EPR spectra recorded from sulfur and Mo precursors was found. This clearly infers that the unreacted compound could not account for the observed EPR spectra. The observed EPR spectra also does not resemble the spectra collected from the Teflon tape, quartz tube and empty cavity.

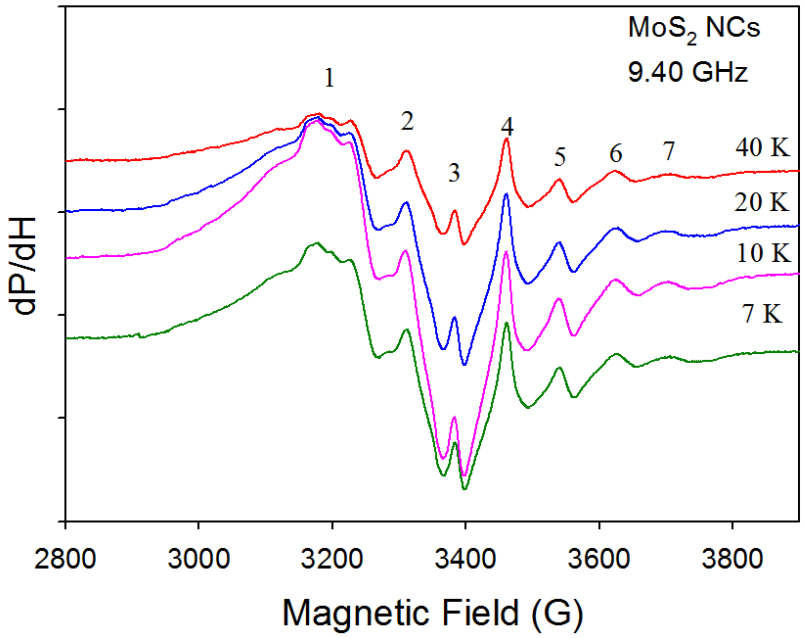

Figure 20: Temperature dependence of MoS_2 NCs at 7, 10, 20 and 40 K.

To better understand the behavior of the observed spin centers, temperature dependent EPR measurements (7 - 40 K) were performed on as prepared MoS_2 nanocrystals, presented in Fig. 20. Furthermore, as presented in Table II and Table III, the g-values and the linewidths of all the EPR lines did not practically vary as a function of increasing temperature 7 – 40 K, consistent with the previous observations [81, 82] in support of Mo^{5+} species, whose EPR spectra was shown to be temperature independent. This leads to believe that these are isolated intrinsic paramagnetic defects, and do not interact with each other.

Now to discuss the possible origin of these paramagnetic defect centers involved in the observed EPR spectra. The signals in the low field region (< 3000 G) are very weak in intensity, also not well resolved compared to the rest of the spectrum. Hence, that part of the spectrum is excluded from the present discussion. Therefore, the efforts of analyzing the signals will be

Table II: g-values of EPR signals shown in Fig. 15

	g values			
	7K	10K	20K	40K
Signal 1	2.1144	2.1152	2.1144	2.1136
Signal 2	2.03	2.03	2.03	2.0298
Signal 3	1.9863	1.9867	1.9867	1.9863
Signal 4	1.9417	1.9423	1.9421	1.9421
Signal 5	1.8984	1.8988	1.8988	1.8984
Signal 6	1.8541	1.8545	1.8538	1.8556
Signal 7	1.8146	1.8153	1.8167	1.8131

focused on the ones labelled 1 to 7 in the spectrum (Fig. 20). Though detected in the XPS spectra, Mo^{6+} is diamagnetic; not expected [82] to give an EPR signal, and hence this possibility can be ruled out. Even though it is paramagnetic and abundant as seen in XPS, Mo^{4+} would give quite broad signal due to large zero field splitting. This possibility can also be ruled out as all the signals observed have relatively narrower line widths ranging from 40 – 96 G. Mo^{3+} is relatively unstable and cannot be captured using X-band EPR. Hence, Mo^{5+} is left, which is paramagnetic, EPR-detectable and highly stable. In the present study, the absolute spin concentrations of all these paramagnetic sites were not derived, as it is not straightforward to estimate, particularly, given the complexity of the spectrum. It might require simulation of the entire powder spectrum that needs usage of computation work and modeling [83, 84], which is beyond the scope of this Thesis.

Table III: Linewidths of EPR signals shown in Fig. 15

	Linewidths			
	7K	10K	20K	40K
Signal 1	91.3	92.62	89.54	86.24
Signal 2	57.42	56.32	58.3	56.76
Signal 3	14.74	14.08	15.62	14.74
Signal 4	63.36	62.92	62.26	64.9
Signal 5	47.96	47.3	46.86	46.2
Signal 6	62.26	63.8	62.26	62.26
Signal 7	47.96	46.64	45.1	51.26

With that respect, to have a better understanding of the EPR spectra found for these samples, the work done [83, 84] by Zanchettta's group in France about 40 years ago on MoS_2

compounds, was recognized to guide this work further. They have prepared these compounds in an entirely different way (thermal decomposition and precipitation methods) than the samples prepared in this work. The work presented by Zanchetta *et al* identified three classes of paramagnetic spin centers with variable intensity, of Lorentzian shape in character. Signal 1, g = 2.114, is assigned to oxygen absorbed species [85] (measurements were performed in open air), though it was not observed in most of the previous studies [86, 87, 83, 84, 88]. Signal 2 is assigned to sulfur chains in the structure, consistent with the observations reported [83] on irradiated amorphous Sulphur, where the electron hole is localized on the sulfur atom. It is noted that this signal is much narrower than that (120 – 150 G) of the similar sulfur-related signals reported in the literature [87, 83, 84, 88]. There is a possibility that this might be due to strong exchange narrowing effect. The EPR lines originating at g = 1.986 and g = 1.9417 (Signal 3 and 4) are argued to come from Mo^{5+} ($4d^1$ configuration) paramagnetic centers surrounded by sulfur environment (MoS_3). The EPR observations appearing at g = 1.898, 1.854 and 1.814 (Signals 5, 6 and 7) were ascribed to Mo^{5+} paramagnetic centers surrounded by oxygen environment (MoO_3). These observations confirm what was hinted at by the XPS measurements.

Section 2 – MoS_2 NCs Annealed with Argon EPR spectra

Annealing MoS_2 nanocrystals under Ar ambience can improve the crystallinity, phase formation, but, at the expense of grain growth. The number of active defect sites are expected to decrease due to the decrease in surface area of MoS_2 nanocrystals upon Ar annealing (4 hours, 300^o C). Looking at the modified EPR spectra after Ar annealing, very distinct paramagnetic centers were found. Interestingly, the rich EPR spectrum observed from MoS_2 nanocrystals disappeared; instead, in Figure 21 a broad signal (g-value = 2.089; peak-to-peak line width = 821 G) and a narrow signal (g-value = 1.928; peak-to-peak line width = 69 G) were observed. Upon

closer inspection, it was noticed that there are a few more weak unresolved narrow signals overriding on the broader signal. This implies that the paramagnetic defect sites observed from pristine MoS_2 nanocrystals still exist, however, with much reduced defect density.

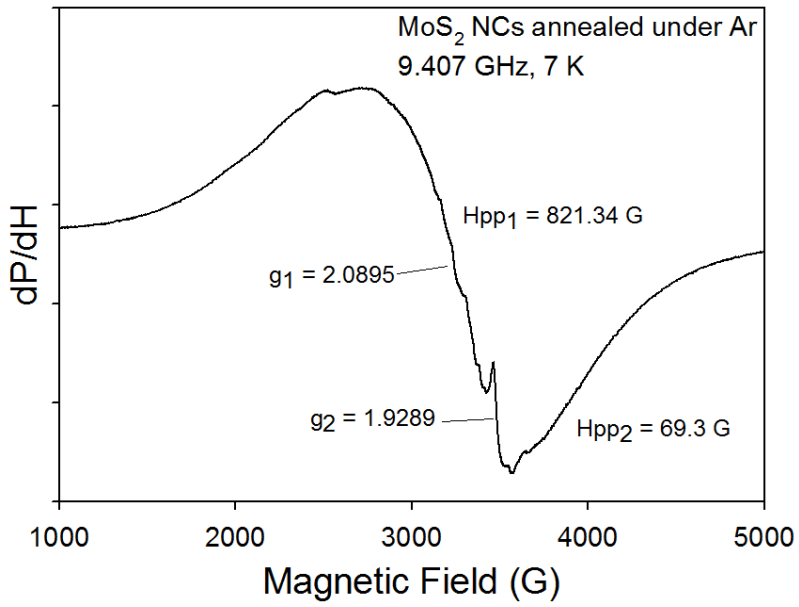

Figure 21: The EPR spectra collected on Ar annealed MoS_2 nanocrystals measured at 7 K.

To trace the origin of the broad signal, the work done by Arcon and co-authors will be used for aid [89]. The authors conducted X-band EPR study on Li doped MoS_2 nanotubes. They observed two quite different components. A broad (800 – 2600 G) signal associated with the g-value of 2.15-2.52 and a narrow (~ 4 G) signal appeared at the g-value of 2.0029 were detected. The fact that the broad signal g-value is farther from the free electron g-value (2.0023) suggests considerable spin-orbit coupling. The authors attributed the broad signal to (d-band) conduction electrons coupled to defects through exchange interaction. As the g-value and line width of the broad signal observed in the present work are in close agreement with their observations, the broad signal in Fig. 21 are assigned to conduction electron spins. It is natural to expect a similar situation that might have occurred in our MoS_2 nanocrystals during the Ar annealing process, which results in significant surface reorganization toward bulk-like structure. On the other hand, the narrower and weaker signal could be assigned to oxo-Mo^{5+} centers, which might be present in the form of small spin clusters. It is evident that this particular oxo-Mo^{5+} site still survived even after Ar annealing treatment. This

finding implies that the observed spin centers are of surface-related, and probably are located on the edges of the layers.

Section 3 – TM doped MoS_2 NCs

Now, why the variations in the magnetic and catalytic properties of the studied materials occur as a function of transition metal doping is discussed. The present work as well as the early-on reports [90-93] showed that the transition metal elements show interesting magnetic properties as well as pronounced catalytic activity. From our experimental observations, it was learned that the Mn doped MoS_2 NCs showed least catalytic performance and showed predominant paramagnetism at room temperature. Whereas the pristine MoS_2 and Co, Ni, and Fe doped MoS_2 NCs showed good catalytic performance as well as stronger room temperature ferromagnetism. To better understand the relationship between the magnetism and catalytic performance, X-band EPR measurements on all the samples at room temperature (300 K) have been performed.

The data is plotted in Figure 22. As it can be clearly noticed, Mn doped MoS_2 NCs did not show signals coming from the catalytically active centers, except the strong signal that comes from Mn^{2+} only. On the other hand, the samples doped with Co, and Ni including undoped MoS_2 NCs showed many sharp EPR signals, indicating the presence of larger number of catalytically active centers. Hence, we believe that Co doped MoS_2 NCs showed superior catalytic performance compared to Mn doped MoS_2 NCs. These active defect centers contain unpaired electron spins due to uncoordinated and dangling bonds. The observed ferromagnetic behavior could have resulted from the interaction between these active spin centers. This may also be due to the formation of MnS (undetected) in the reaction yield, which changes the 2D structure of MoS_2 nanolayers to 3D, and causes the electrocatalytic properties to deteriorate [94]. The EPR spectra of MoS_2 NCs has

been analyzed and identified the active defect centers in a previous chapter. Detailed analysis of the EPR spectra collected from transition metal doped MoS_2 NCs is being performed.

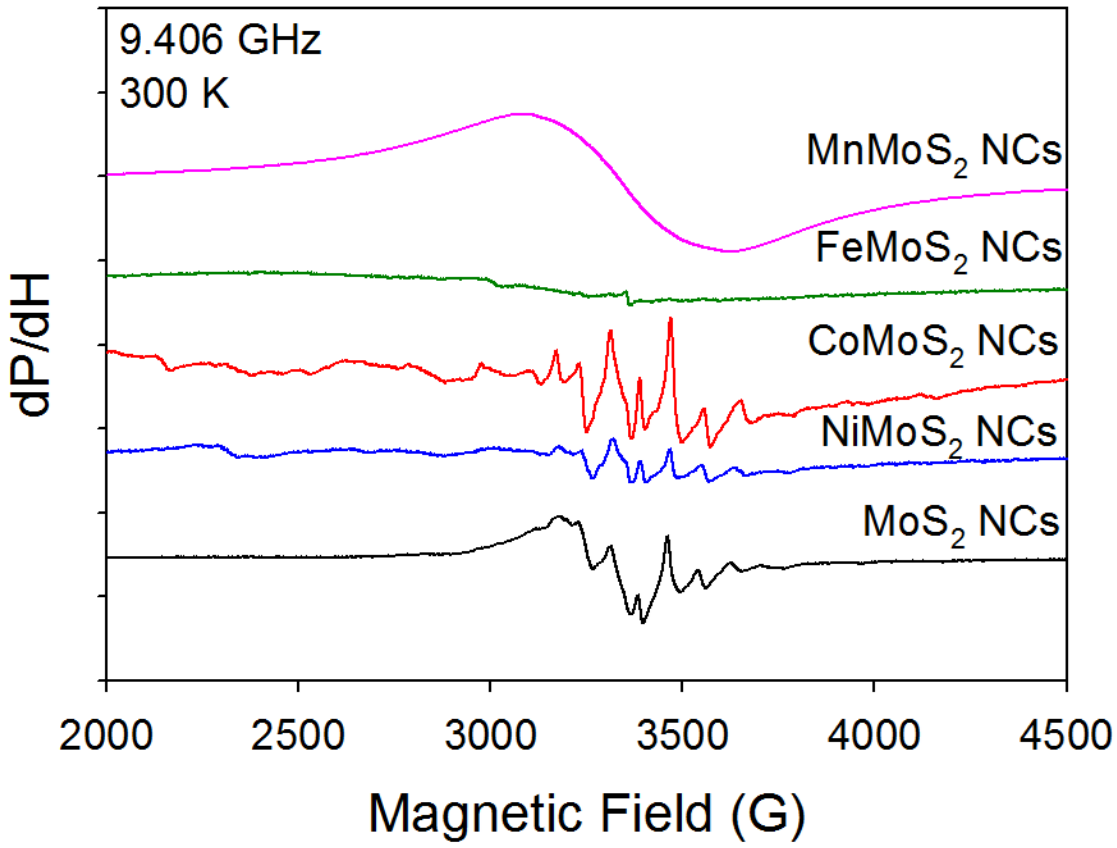

Figure 22: X-band room temperature (300 K) EPR spectra collected from MoS_2, Co, Ni, Fe and Mn doped MoS_2 NCs.

Conclusion

To conclude, in this thesis, we have reported the magnetic and catalytic properties of hydrothermally grown transition metal doped (10% of Co, Ni, Fe and Mn) MoS_2 NCs associated with the particle size of 25-30 nm. Interestingly, the undoped MoS_2 NCs showed a mixture of canted anti-ferromagnetic and ferromagnetic behavior. MoS_2 NCs doped with Co, Ni, and Fe exhibited profound room temperature paramagnetic nature, predominantly. For all the materials, modified CW law described the temperature dependent magnetic behavior, and the ground state is canted antiferromagnetic phase associated with uncompensated electron spins. In addition, we have also studied the hydrogen evolution reaction performance. The present study compared the current densities (j), measured at the over potentials of $-372.8\ mV \leq \eta \leq -169.6\ mV$, listed from greatest to least, $j(FeMoS_2) = 4.05$, $j(CoMoS_2) = 3.00$, $j(MoS_2) = 2.09$, $j(NiMoS_2) = 1.5$ mA/cm2, and $j(MnMoS_2) = 52$ μA/cm2. The order of the overall reaction activity is obtained from Tafel slopes as $CoMoS_2 > MoS_2 > NiMoS_2 > FeMoS_2 > MnMoS_2$. The electrochemical impedance spectroscopic measurements indicated that Fe doped MoS_2 NCs have the best conductivity and charge transfer ability, while Mn-doped MoS_2 had the lowest. More likely, it is due to the creation of more number of catalytically active centers in Co doped MoS_2 NCs compared to Mn doped MoS_2 NCs evidenced from room temperature EPR measurements. This could be due to Co modifying the activity of the S-edge. Additional work is in progress to establish the relationship between the magnetic and catalytic properties of these materials.

Future Directions

Magnetic and catalytic properties will be performed in the immediate future to understand the effects of annealing these materials under various gas environments, and apply to possible gas sensing applications. Low temperature EPR studies will also be performed for the transition metal doped MoS_2 NCs. Plans of simulating the entire EPR powder spectra of the TM doped MoS_2 NCs are in the future to fully grasp all the interactions within the materials. Lastly, a comparison of the magnetic properties of MoS_2 with other 2D layered materials such as; VS_2 and VSe_2 will be performed.

References

1) Q. H. Wang, K. Kalantar-Zadeh, A. Kis, **Electronics and optoelectronics of two-dimensional transition metal dichalcogenides**, Nat. Nanotech., 7, 699 (2012)

2) G. R. Bhimanapati, Z. Lin, V. Meunier, Y. Jung, J. Cha, **Recent Advances in Two-Dimensional Materials Beyond Graphene**, ACS Nano 12, 11509 (2015)

3) S. Z. Butler, S. M. Hollen, L. Cao, Y. Cui, J. A. Gupta, **Progress, Challenges, and Opportunities in Two-Dimensional Materials Beyond Graphene**, ACS Nano 12, 2898 (2013)

4) K. F. Mak, C. Lee, J. Hone, J. Shan, T. F. Heinz, **Atomically Thin MoS2: A New Direct-Gap semiconductor**, PRL 105, 136805 (2010)

5) S. Ahmed, X. Ding, N. Bao, P. Bian, R. Zheng, Y. Wang, **Inducing high coercivity in MoS2 nanosheets by transition element doping,** Chem. Mater. 29, 21, 9066 (2017)

6) G. Ye, Y. Gong, J. Lin, B. Li, Y. He, **Defects Engineered Monolayer MoS2 for Improved Hydrogen Evolution Reaction**, Nano Lett., 16, 1097 (2016)

7) G. Li, D. Zhang, Q. Qiao, Y. Yu, D. Peterson, **All The Catalytic Active Sites of MoS2 for Hydrogen Evolution**, J. Am. Chem. Soc., 138, 16632 (2016)

8) Y. Yu, S. Y. Huang, Y. Li, S. N Steinmann, **Layer-Dependent Electrocatalysis of MoS2 for Hydrogen Evolution**, Nano Lett., 14, 553 (2014)

9) T. F. Jaramillo, K. P. Jorgensen, J. Bonde, **Identification of Active Edge Sites For Electrochemical H2 Evolution from MoS2 nanocatalysts**, Science, 317, 100 (2007)

10) Y. Xu, L. Wang, S. Zhang, C. Liu, **Monolayer MoS_2 with S vacancies from interlayer spacing expanded counterparts for highly efficient electrochemical hydrogen production**, J. Mater. Chem. A, 4, 16524 (2016)

11) Y. Wu, M. Zarei-Chaleshtori, B. Torres, T. Akter, C. Diaz-Moreno, G. B. Saupe, J. A. Lopez, R.R. Chianelli, D. Villagran, **Electrocatalytic hydrogen gas generation by cobalt molybdenum disulfide (CoMoS2) synthesized using alkyl-containing thiomolybdate precursors,** Int. J. Hydrogen Energy 42, 20669 (2017)

12) M. Chhetri, U. Gupta, L. Yadgarov, R. Rosentsveig, R. Tenne, C. N. R. Rao, **Beneficial effect of Re doping on the electrochemical HER activity of MoS2 fullerenes**, Dalton Trans., 44, 16399 (2015)

13) H. Wang, C. Tsai, D. Kong, **Transtion-metal doped edge sites in vertically aligned MoS2 catalysts for enhanced hydrogen evolution,** Nano Res., 8, 2, 566 (2015)

14) Y. Yin, J. Han, **Contributions of Phase, Sulfur Vacancies, and Edges to the Hydrogen Evolution Reaction Catalytic Activity of Porous Molybdenum Disulfide Nanosheets**, J. Am. Chem. Soc., 138, 7965 (2016)

15) X. Dai, **Co-Doped MoS_2 Nanosheets with the Dominant CoMoS Phase Coated on Carbon as an Excellent Electrocatalyst for Hydrogen Evolution,** ACS Appl. Mater. Interfaces, 7 , 27242 (2015)

16) Z. C. Xiang, Z. Zhang, X. Xu, Q. Zhang, Q. Wang, C. Yuan, **Room-temperature ferromagnetism in Co doped MoS2 sheets,** Phys. Chem. Chem. Phys., 17, 15822 (2015)

17) J. D. Fuhr, A. Saul, **Scanning Tunneling Microscopy Chemical Signature of Point Defects on the MoS2 (0001) Surface,** Phys. Rev. Lett., 92, 026802, (2004)

18) S. Yan, W. Qiao, X. He, X. Guo, L. Xi, W. Zhong, Y. Du, **Enhancement of magnetism by structural phase transition in MoS2,** Appl. Phys. Lett. 106, 012408 (2015)

19) A. A. Tedstone, D. J. Lewis, P. O'Brien, **Synthesis, Properties, and Applications of Transition Metal-Doped Layered Transition Metal Dichalcogenides,** Chem. Mater. 28, 1965 (2016)

20) H. D. Xia, H. P. Li, C. Y. Lan, C. Li, X. X. Zhang, S. J. Zhang, Y. Liu, **Ultrafast erbium-doped fiber laser mode-locked by a CVD-grown molybdenum disulfide (MoS_2) saturable absorber,** Opt. Express, 22, 17341 (2014)

21) A. Ayari E. Cobas, O. Ogundadegbe, M. S. Fuhrer, **Realization and electrical characterization of ultrathin crystals of layered transition-metal dichalcogenides,** J. Appl. Phys., 101, 14507 (2007)

22) X. B. Fan, P. T. Xu, D. K. Zhou, Y. F. Sun, Y. G. C. Li, M. A. T. Nguyen, M. Terrones, T. E. Mallouk, **Fast and Efficient Preparation of Exfoliated 2H MoS_2 Nanosheets by Sonication-Assisted Lithium Intercalation and Infrared Laser-Induced 1T to 2H Phase Reversion**, Nano Lett., 15, 5956 (2015)

23) L. M. Martinez, M. D. Teran, R. R. Chianelli, S. R. J. Hennadige, S. R. Singamaneni, **Magnetic Defects in Transitional Metal Di-chalcogenide semiconducting materials,** MRS Adv., 3, 6-7, 351 (2018)

24) L. M. Martinez, C. Karthik, M. Kongora, S. R. Singamaneni, **Paramagnetic Defects in Hydrothermally Grown Few-Layered MoS2 Nanocrystals,** J. Mat. Res., Accepted (2018)

25) D. Gao, M. Si, J. Li, J. Zhang, Z. Zhang, Z. Yang and D. Xue, **Ferromagnetism in freestanding MoS_2 nanosheets**, Nanoscale Res. Lett., **8**, 129 (2013).

26) R. Zhang, Y. Li, J. Qi and D. Gao, **Ferromagnetism in ultrathin MoS_2 nanosheets: from amorphous to crystalline**, Nanoscale Res. Lett., **9,** 586 (2014).

27) Ojha, S. Saha, S. Banerjee, A. K. Ganguli, **Efficient electrocatalytic hydrogen evolution from MoS2-functionalized Mo2N Nanostructures**, ACS Appl. Mater. Interfaces **9**, 19455 (2017)

28) B. Yoosuk, J. H. Kim, C. Song, C. Ngamcharussrivichai, P. Prasassarakich, **Higly active MoS2, CoMoS2 and NiMOS2 unsupported catalysts prepared by hydrothermal synthesis for hydrodesulfurization of 4,6-dimethyldibenzothiophene,** Cat. Tod., 130, 14 (2008)

29) C. Wivel, R. Candia, B. S. Clausen, S. Morup, H. Topsoe, **On the catalytic significance of a C-Mo-S Phase in Co-MoAl2O3 Hydrodesulfurizatin Catalysts: Combined in situ Mossbauer Emission Spectroscopy and Activity Studies,** J. Catal., 68, 453 (1981)

30) J. Kibsgaard, Z. Chen, B. N. Reinecke, and T. F. Jaramillo, **Engineering the surface structure of MoS_2 to preferentially expose active edge sites for electrocatalysis**, Nature Mater., **11,** 963 (2012).

31) T. F. Jaramillo, K. P. Jørgensen, J. Bonde, J. H. Nielsen, S. Horch, I. Chorkendorff, **Identification of Active Edge Sites for Electrochemical H_2 Evolution from MoS_2 Nanocatalysts**, Science **317**, 100 (2007).

32) Y. Yu, S-Y Huang,Y. Li, S. N. Steinmann, W. Yang, and L. Cao, **Layer-Dependent Electrocatalysis of MoS_2 for Hydrogen Evolution**, Nano Lett., **14**, 553 (2014).

33) B. Hinnemann, P. G. Moses, J. L. Bonde, K. P. Jørgensen, J. H. Nielsen, S. Horch, I. Chorkendorff, J. K. Nørskov, **Biomimetic Hydrogen Evolution: MoS_2 Nanoparticles as Catalyst for Hydrogen Evolution**, J. Am. Chem. Soc., **127**, 5308, (2005).

34) H. Wang, C. Tsai, D. Kong, K. Chan, F. Abild-Pedersen, J. K. Nørskov, Y. Cui, **Transition-metal doped edge sites in vertically aligned MoS_2 catalysts for enhanced hydrogen evolution**, Nano Res., **8**, 566 (2015).

35) G. Liu, A. W. Robertson, M. Meng-Jung Li, W. C. H. Kuo, M. T. Darby, M. H. Muhieddine, Y-C Lin, K. Suenaga, M. Stamatakis, J. H. Warner and S. C. E. Tsang, **MoS_2 monolayer catalyst doped with isolated Co atoms for the hydrodeoxygenation reaction**, Nature Chem., **9**, 810 (2017).

36) Z. Xiang, Z. Zhang, X. Xu, Q. Zhang, **Room-temperature ferromagnetism in Co doped MoS2 sheets**, Phys. Chem. Chem. Phys., 17, 15822 (2015)

37) P.A. Spevack and N.S.Mclntyre, **A Raman and XPS investigation of supported molybdenum oxide thin films. 2. Reactions with hydrogen sulfide**, J. Phys. Chem., **97**, 11031 (1993).

38) W. Zhang, T. Zhou, J. Zheng, J. Hong, Y. Pan, R. Xu, **Water-Soluble MoS_3 Nanoparticles for Photocatalytic H2 Evolution**, ChemSusChem, **8**, 1464 (2015)

39) L. M. Martinez, J. Delgado, C. Saiz, A. Cosio, Y. Wu, D. Villagran, K. Gandha, I. Nlebedim, S. R. Singamaneni, **Magnetic and Electrocatalytic Properties of Transition Metal Doped MoS2 Nanocrystals,** J. Phys. Chem. C, Under Review (2018)

40) J. M. Thomas, I. Adams, R. H. Williams, M. Barber, **Valence band structures and core-electron energy levels in the monochalcogenides of gallium. Photoelectron spectroscopic study,** J. Chem. Soc. Faraday, Trans II 68, 755 (1972).

41) J. E. Devries, H. C. Yao, R. J. Baird, H. S. Gandhi, **Characterization of molybdenum platinum catalysts supported on γ-alumina by X-ray photoelectron spectroscopy,** J. Catal. 84, 8 (1983).

42) N. H. Turner, A. M. Single, **Determination of peak positions and areas from wide-scan XPS spectra,** Surf. Interface and 15, 215 (1990).

43) L. Benoist, D. Gonbeau, G. Pfister-Guillouzo, E. Schimidt, G. Meunier, A. Levasseur, **X-ray photoelectron spectroscopy characterization of amorphous molybdenum oxysulfide thin films,** Thin Solid Films 258, 110 (1995).

44) N. S. Mc Intyre, D. D. Johnston, L. L. Coatsworth, R. D. Davidson, J. R. Brown, **X-ray photoelectron spectroscopic studies of thin film oxides of cobalt and molybdenum,** Surf. Interface Anal. 15, 265 (1990).

45) F. S. Khumalo, C. G. Olson, J. W. Anderegg, D.W. Lynch, **Optical transitions, XPS, electronic states in NiPS3,** Chem. Phys. 65, 289 (1982).

46) B. Brox, I. Olefjord, **ESCA studies of MoO2 and MoO3,** Surf. Interface Anal. 13, 3 (1988).

47) I. Alstrup, I. Chorkendorff, R. Candia, B. S. Clausen, H. Topsoe, **A combined X-ray photoelectron and Mossbauer emission spectroscopy study of the state of cobalt in sulfide, supported, and unsupported Co-Mo catalysts,** J. Catal. 77, 397 (1982).

48) H. M. Wu, S. A. Chen, **Dopant-polymer interaction: $MoCl^{5-}$ doped polyacetylene,** Synthetic Metals 26, 225 (1988).

49) S. J. Hilsenbenk, V. G. Young Jr., R. E. McCarley, **Synthesis, structure, and characterization of N-ligated Mo6S8L6 cluster complexes. Molecular precursors to Chevrel phases,** Inorg. Chem. 33, 1822 (1994).

50) J. T. Roberts, C. M. Friend, **Desulfurization of ethylene sulfide on Mo(100): The roles of ring size and strain in adsorbate reaction selectivity,** Surf. Sci. 202, 405 (1988).

51) X. R. Yu, F. Liu, Z. Y. Wang, Y. Chen, **Auger parameters for sulfur-containing compounds using a mixed aluminum-silver excitation source,** J. Electron Spectrosc. Relat. Phenom. 50, 159 (1990).

52) D. R. Mullins, D. R. Huntley, S. H. Overbury, **The nature of the sulfur induced surface reconstruction on Ni (111),** Surf. Sci. 323, L287 (1995).

53) C. Battistoni, L. Gastaldi, A. Lapiccirella, G. Mattongo, C. Viticoli, **Octahedral vs tetrahedral coordination of the Co (II) ion in layer compounds: CoxZn1-xIn2S4 (0<x<0.46) solid solution,** J. Phys. Chem. Solids 47, 899 (1986).

54) R. B. Shalvoy, P. J. Reucroft, **Characterization of a sulfur-resistant methanation catalyst by XPS,** J. Vac. Sci. Technol. 16, 567 (1979).

55) G. M. Bremmer, L.van Haandel, E. J. Hensen, J. W. M. Frenken, P. J. Kooyman, **Instability of NiMoS2 and CoMoS2 Hydrodesulfurization Catalysts at ambient conditions: a quasi in Situ High resolution Transmission Electron microscopy and XPS study**, J. Phys. Chem. C 120, 34, 19204 (2016).

56) D. Wang, X. Zhang, Y. Shen, Z. Wu, **Ni-doped MoS2 nanoparticles as highly active hydrogen evolution electrocatalysts,** RSC Adv., 6, 16656 (2016).

57) H. Van der Heide, R. Hemmel, C. F. Van Bruggen, C. Haas, **X-ray photoelectron spectra of 3d transition metal pyrites,** J. Solid State Chem. 33, 17 (1980).

58) N. S. McIntyre, M. G. Cook, **X-ray photoelectron studies on some oxides and hydrooxides of cobalt, nickel, and copper,** Anal. Chem. 47, 2208 (1975).

59) P.A. Spevack and N.S.Mclntyre, **A Raman and XPS investigation of supported molybdenum oxide thin films. 1. Calcination and reduction studies**, J. of Phys. Chem., **97**, 11020 (1993).

60) D. Gao, M. Si, J. Li, J. Zhang, Z. Zhang, Z. Yang, D, Xue, **Ferromagnetism in freestanding MoS_2 nanosheets**, Nanoscale Res. Lett., **8**, 129 (2013).

61) S. Yan, W. Qiao, X. He, X. Guo, L. Xi, W. Zhong, Y. Du, **Enhancement of magnetism by structural phase transition in MoS_2**, Appl. Phys. Lett., **106**, 012408 (2015)

62) J. Wang, F. Sun, S. Yang, Y. Li, C. Zhao, M. Xu, Y. Zhang, H. Zeng, **Robust ferromagnetism in Mn-doped MoS_2 nanostructures**, Appl. Phys. Lett., **109**, 092401 (2016).

63) S. S. Rao, S. Narayana Jammalamadaka, A. Stesmans, V. V. Moshchalkov, J. van Tol, D. V. Kosynkin, A. Higginbotham, J. M. Tour, **Ferromagnetism in Graphene Nanoribbons: Split Versus Oxidative Unzipped Ribbons**, Nano Letters **12**, 1210 (2012).

64) J. Zhang, J. M. Soon, K. P. Loh, J. Yin, J. Ding, M. B. Sullivian, P. Wu, **Magnetic Molybdenum Disulfide Nanosheet Films**, Nano Lett. **7**, 2370 (2007).

65) Z. C. Xiang, Z. Zhang, X. J. Xu, Q. Zhang, Q. B. Wang, C. Yuan, **Room-temperature ferromagnetism in Co doped MoS_2 sheets**, Phys. Chem. Chem. Phys.,**17**, 15822 (2015).

66) B. Xia, Q. Guo, D. Gao, S. Shi, K. Tao, **High temperature ferromagnetism in Cu-doped MoS_2 nanosheets**, J. Phys. D, Appl. Phys. **49** 165003 (2016)

67) S. Ahmed, X. Ding, N. Bao, P. Bian, R. Zheng, Y. Wang, P. P. Murmu, J. V. Kennedy, R. Liu, H. Fan, K. Suzuki, J. Ding, J. Yi, **Inducing High Coercivity in MoS2 Nanosheets by Transition Element Doping**, Chem. Mater., **29**, 9066 (2017).

68) B. Xia, Y. Yang, J. Ma, K. Tao, D. Gao, **Adjustable Ferromagnetic Behavior in Iron-Doped Two-Dimensional MoS_2 Multilayer Nanosheets**, Appl. Phys. Express, **10**, 09332 (2017).

69) K. P. Bhatti, S. Chaudhary, D. K. Pandya, S. C. Kashyap, **Intrinsic and extrinsic origin of room temperature ferromagnetism in ZnO:Co**, J. Appl. Phys. **101**, 103919 (2007)

70) D. Wang, X. Zhang, Y. Shen and Z. Wu, **Ni-doped MoS2 nanoparticles as highly active hydrogen evolution electrocatalysts**, RSC Adv., 6, 16656 (2016)

71) S. Dong, X. Liu, X. Li, V. Kanzyuba, T. Yoo, S. Rouvimov, S. Vishwanath, H. G. Xing, D. Jena, M. Dobrowolska, J. K. Furdyna, **Room temperature weak ferromagnetism in $Sn_{1-x}Mn_xSe_2$ 2D films grown by molecular beam epitaxy**, APL MATERIALS **4**, 032601 (2016)

72) C. S. Park, D. Chu, Y. Shon, J. Lee, E. K. Kim, **Room temperature ferromagnetic and ambipolar behaviors of MoS_2 doped by manganese oxide using an electrochemical method**, Appl. Phys. Lett, **110**, 222104 (2017)

73) J. Deng, H. Li, J. Xiao, Y. Tu, D. Deng, H. Yang, H. Tian, J. Li, P. Ren, X. Bao, **Triggering the electrocatalytic hydrogen evolution activity of the inert two-dimensional MoS_2 surface via single-atom metal doping**, Energy Environ. Sci., **8**, 1594 (2015).

74) X. Ren, L. Pang, Y. Zhang, Xiaodong Ren, H. Fan, **One-step hydrothermal synthesis of monolayer MoS_2 quantum dots for highly efficient electrocatalytic hydrogen evolution**, J. Mater. Chem. A, **3**, 10693 (2015).

75) K. Ojha, S. Saha, S. Banerjee, A. K. Ganguli, **Efficient Electrocatalytic Hydrogen Evolution from MoS_2-Functionalized Mo_2N Nanostructures**, ACS Appl. Mater. Interfaces, **9**, 19455 (2017).

76) X. Dai, K. Du, Z. Li, M. Liu, Y. Ma, H. Sun, X. Zhang, **Co-Doped MoS_2 Nanosheets with the Dominant CoMoS Phase Coated on Carbon as an Excellent Electrocatalyst for Hydrogen Evolution**, ACS Appl. Mater. Interfaces, **7**, 27242-27253 (2015).

77) Prins, R.; De Beer, V. H. J.; Somorjai, G. A., **Structure and Function of the Catalyst and the Promoter in Co – Mo Hydrodesulfurization Catalysts**, Cat. Rev., **31**, 1 (1989).

78) J.W.C.Spackman, **Electron spin resonance of charge carriers in impure molybdenum disulphide**, Nature, **198**, 1266 (1963).

79) F. D. Brand, G. M. Ribeiro, P. H. Vaz, J. C. Gonz_alez, K. Krambrock, **Identification of rhenium donors and sulfur vacancy acceptors in layered MoS_2 bulk Samples**, J. Appl. Phys. **119**, 235701 (2016).

80) A. Stesmans, S. Iacovo, V. V. Afanas'ev, **ESR study of p-type natural 2H-polytype MoS_2 crystals: The As acceptor activity**, Appl. Phys. Lett., **109**, 172104 (2016).

81) A.J.A. Konings, A.M. van Doormen, D.C.Koningsberger, V.H.J. De Beer, A. L. Farragher, G.C.A. Schuit, **ESR Studies on Hydrodesulfurization Catalysts: Supported and unsupported Sulfided Molybdenum and Tungsten Catalysts**, J. of Catalysis **54**, 1 (1978).

82) K.C.Khulbe, R.S. Mann, M. Ternan, **Electron spin resonance of the surface chemistry of molybdenum-alumina catalysts**, CAN. J. CHEM **56**, 1769 (1978).

83) Y. Bensimon, P. Belougne, J. C. Giuntini, J. V. Zanchetta, **Electron Spin Resonance of Water Adsorption on Amorphous Molybdenum Sulfide**, J. Phys. Chem. **88**, 2754 (1984)

84) B. Deroide, Y. Bensimon, P. Belougne, J. V. Zanchetta, **Lineshapes of ESR signals and the nature of paramagnetic species in amorphous molybdenum sulfides**, J. Phys. Chem. Solids **52,** 853, (1991)

85) A. Sobczynski, Zmierczak, **Characterization of MoS2/SiO2 by ESR and NO absorption**, React. Kinet. Catal. Lett., **44**, 511 (1991).

86) K. C. Khulber, S. Mann, and M. Ternan, **Electron spin resonance studies of the surface chemistry of molybdenum-alumina catalysts**, Can. J. Chem. **56**, 1769 (1978).

87) B. G. Silbernagel, T. A. Pecoraro, R. R. Chianelli, **Electron Spin Resonance of Supported and Unsupported Molybdenum Hydrotreating Catalysts**, J. Catalysis **78**, 380 (1982).

88) C. Louis, M. Che, **EPR Investigation of the Coordination Sphere of Mo^{5+} Ions on Thermally Reduced Silica-Supported Molybdenum Catalysts Prepared by the Grafting Method**, J. Phys. Chem., **91**, 2875 (1987).

89) D. Arcon, A. Zorko, P. Cevc, A. Mrzel, M. Remsˇkar, R. Dominko, M. Gabersˇcˇek, and D. Mihailovic, **Electron spin resonance of doped chalcogenide nanotubes**, Phys. Rev. B, **67**, 125423 (2003).

90) P. W. Selwood, **Magnetism and Catalysis**, *Chem. Rev.*, **38** (1), 41 (1946).

91) J. T. Richardson, **Magnetism and catalysis**, J. Appl. Phys., **49**, 1781 (1978)

92) R. J. H. Voorhoeve, **Experimental Relationships between Catalysis and Magnetism,** AIP Conference Proceedings, **18**, 19 (1974).

93) E. Torun, C. Fang, M. de Wijs, R. A. de Groot, **Role of Magnetism in Catalysis: RuO_2 (110) Surface**, J. Phys. Chem. C., **117**, 6353-6357 (2013).

94) Aleksander A. Tedstone, David J. Lewis, Paul O'Brien, **Synthesis, Properties, and Applications of Transition Metal-Doped Layered Transition Metal Dichalcogenides**, Chem. Mater., **28**, 1965−1974 (2016).

Curriculum Vita

My name is Luis M. Martinez Milian. I started my journey through science doing an Associate's Degree in Technology for Electronics in my Alma Mater, University of Puerto Rico at Humacao (UPRH). During that time I found a deep appreciation for Physics thanks to the teachings of a professor from back home. After completing my Associate's, I moved on the do my B.S. in Physics applied to Electronics at UPRH. There I developed myself as a fledgling scientist doing volunteer research work with several professors. From learning to use the Electrospinning technique to produce PVDF nanofibers, to helping develop and later race a moonbuggy for the NASA annual moonbuggy race. After a few years in my B.S. I applied to the PREM program in UPRH and got accepted to work alongside Dr. N. Pinto. With him, I learned various techniques and skills which have helped throughout my Master's degree. I was able to present two poster presentations through the PREM program in UPRH in a conference and symposium. I am truly grateful for the experiences I had during my time in UPRH.

Currently, I'm finishing my Master's degree in Physics here at the University of Texas at El Paso. While doing my Master's, was granted the chance to become a Teaching Assistant. This has helped me view things through an educators eyes and I can appreciate the work performed to pass on knowledge. In UTEP I also met Dr. Rao, my current advisor, whom has taught me to become a better researcher than who I was before. With his help, I have been able to publish five papers. Two of which are on my main project. I have also been able to present my work in several conferences as poster and oral presentations. For this, I thank my advisor for granting me the tools I need to move forward.